國立臺灣大學理學院物理學系

博士論文

Department of Physics

College of Science

National Taiwan University

Doctoral Dissertation

奈米金屬球殼表面電漿共振之研究

Study of surface plasmon resonance for metallic nanoshells

鍾弘毅

Hung Yi Chung

指導教授：蔡定平 博士

Advisor: Din Ping Tsai, Ph.D.

中華民國 99 年 6 月

Jun, 2010

國立臺灣大學博士學位論文
口試委員會審定書

奈米金屬球殼表面電漿共振之研究
Study of surface plasmon resonance for metallic nanoshells

本論文係鍾弘毅君（D96222002）在國立臺灣大學物理學系、所完成之博士學位論文，於民國九十九年六月五日承下列考試委員審查通過及口試及格，特此證明

口試委員：

蔡定平（簽名）

（指導教授）

M Mai

胡崇德　郭光宇

藍永強　周趙遠鳳

Publications

1. H. Y. Chung, P. T. Leung, and D. P. Tsai, *Dynamic modifications of polarizability for large metallic spheroidal nanoshells*, J. Chem. Phys. **131**, 124122 (2009)
2. H. Y. Chung, H. Y. Xie, P. T. Leung, and D. P. Tsai, *Optical properties of metallic nanoshell composites: The effects of temperature and particle clustering*, Solid State commu. **149**, 2151 (2009)
3. H. Y. Xie, H. Y. Chung, P. T. Leung, and D. P. Tsai, *Plasmonic enhancement of Förster energy transfer between two molecules in the vicinity of a metallic nanoparticle: Nonlocal optical effects*, Phys. Rev. B **80**, 155448 (2009)
4. C. W. Chen, H. Y. Chung, H. P. Chiang, J. Y. Lu, R. Chang, D. P. Tsai, and P. T. Leung, *Nonlocality and particle-clustering effects on the optical response of composite materials with metallic nanoparticles*, Appl. Phys. A (in press)
5. H. Y. Chung, P. T. Leung, and D. P. Tsai, *Enhanced intermolecular energy transfer in the vicinity of a plasmonic nanorice*, Plasmonics (in press)

誌謝

我有一個很好很好的運氣，不知道是誰幫我安排好了，博士班這三年，給了我一個美好的經驗。未來總是未知的，我能做的有限，雖然如此，但在背後幫忙我的人，卻能在黑暗中為我照亮前方的道路。

感謝我的指導教授—蔡定平教授，謝謝他帶我走過博士班這三年，從他不斷努力，不斷的幫助別人，教導了我正確的人生價值是什麼。謝謝老師在我什麼都不會的情況下收我做學生，再一步一步的教導我如何面對問題，如何做研究，引導我走向正確的方向。

藉由老師的介紹，我認識了梁培德教授，在他身上，我看到的是對研究的熱忱，那種源源不絕的熱情，不受年齡所限制。和他合作的那段時間，讓我感受到研究中快樂，這麼單純的快樂卻是如此迷人。梁老師對學生真心的付出，告訴我正確的研究態度，讓我覺得能夠跟著他學習真好。

我要感謝實驗室的同學，謝謝你們組成了這個可愛的實驗室，讓我這三年來不會感到孤單。另外，也謝謝實驗室的林筱瑄小姐和李淑芳小姐，有妳們的幫忙真的太好了。

樂透不會連中兩次，但我真的很幸運，付出很少，卻得到很多！希望蔡老師、梁老師和兩位師母身體健康、事事順心；也希望實驗室的同學們未來一帆風順。

鍾弘毅

2010/6/21

摘要

首先，我們將介紹一種不同於混雜理論的等效場理論，特別用來處理金屬球殼粒子。與混雜理論不同的是，這個等效場理論不把自由電子當成自由流體，再以 Lagrangian 的力學方式去解，而是採用一種等效介質的想法，加上電動力學中的邊界問題的唯一性條件，有系統的求出金屬球殼粒子的極化率，再由此極化率，我們可以得出這個金屬球殼粒子的表面電漿共振波長。

接下來，利用這個等效場理論研究電偶與電偶之間的交互作用，特別是當這一對電偶在靠近金屬球殼時。我們可以觀察到其交互作用會隨著金屬球殼上的表面電漿之鍵結與反鍵結膜態有巨大的加強效果。

最後，利用這樣的等效場理論，我們考慮奈米金屬球殼粒子的混合體，觀察不同的溫度與不同幾合分佈對此混合體的影響。我們發現，有一個特別的共振膜態不受混合體幾何分佈影響，且只出現在金屬球殼粒子中，在實心金屬球中不出現。

Abstract

First of all, we present an approach alternative to the hybridization model for the treatment of the coupled interfacial plasmon modes in metallic nanoshells. Rather than formulating the problem form the Lagrangian dynamics of the free electronic fluid, we adopt an effective medium approach together with the uniqueness of the solutions to electromagnetic boundary value problem, from which the polarizability of the shells can then be systematically and efficiently derived; and the resonance frequencies for the coupled modes can be obtained from the poles in the polarizability.

Secondly, by using this effective medium theory we study the modified dipole-dipole interaction between the molecules in the vicinity of a spheroidal metallic nanoshell. From which huge enhancement of the energy transfer rate is obtained due to the resonant excitation of the bounding and anti-bounding plasmonic modes of the nanoshell.

Finally, we study the optical properties of a metallic nanoshell composite with particular focus on the effects of variation in temperature and particle clustering on these properties. One unique result from our modeling is the persistent manifestation of the single-particle resonances of the individual nanoshells which cannot be found in a composite of solid particles.

Table of Contents

摘要 i

Abstract iii

Table of Figures vii

Chapter 1 Introduction 1

Chapter 2 Polarizability 3

2.1 Polarizability for a spherical particle 3

2.2 Prolate spheroidal coordinates 4

2.3 Polarizability of a prolate spheroidal particle 9

2.4 The polarizability of a core-shell particle 10

2.5 Dipolar and spherical limits for the spheroidal shells 15

2.6 Multi-layered spheroidal “nanomatryushka” 16

Chapter 3 Dynamic Effects 19

3.1 Mie theory 19

3.2 Modify long wavelength approximation 24

3.3 MLWA for spheroidal nanoshells 26

3.4 Improvements on MLWA 30

3.5 Numerical results 31

3.6 Discussion and Conclusion 40

Chapter 4 Förster resonance energy transfer 43

4.1 Introduction 43

4.2 Theoretical model 45

4.3 Numerical results 51

4.4 Conclusion 56

Chapter 5 Metallic Nanoshell Composites 59

5.1 Introduction 59

5.2 Theoretical model 60

5.3 Numerical results 64

5.4 Conclusion 71

Chapter 6 Summary and outlook 73

Bibliography 77

Table of Figures

Figure 2.1 Two types of spheroid: (a) oblate and (b) prolate spheroid. f is the focal lengh. 5

Figure 2.2 Illustration of the approach of the LSC model. 11

Figure 2.3 Coupled resonance modes, $m=0$ and $m=1$, of a confocal prolate metallic nanoshell as a function of the aspect ratio of the core. 14

Figure 3.1 Comparison of the extinction cross sections obtained from the static limit, from MLWA, and from IMLWA against the exact Mie theory results. The results are shown for a spherical nanoshell with inner radius r_1 and outer radius r_2 which are shown on the plots. The silver nanoshell is hollow inside and placed in vacuum. 32

Figure 3.2 Comparison of the extinction cross sections obtained in the static limit, from MLWA, and from IMLWA. The results are shown for a confocal prolate metallic shell with 40 nm foci and aspect ratios 1/2 (core) and 2/3 (outer surface). The nanoshell has a hematite core ($\varepsilon = 9.5$) with the silver shell embedded in vacuum. The electric field is along the rotational symmetry axis of the spheroidal nanoshell. 35

Figure 3.3 The extinction cross section of the confocal prolate metallic nanoshells (foci is fixed at 40 nm) with a fixed aspect ratio (2/3) for the outer surface and four different aspect ratios (0.2, 0.5, 0.55, and 0.6) for the core. The nanoshell has a hematite core ($\varepsilon = 9.5$) with the silver shell embedded in the vacuum. The electric fields are oriented parallel (a) and perpendicular (b) to the rotational symmetry axis of the spheroidal nanoshell. The calculation is based on the MLWA model. 37

Figure 3.4 coupled resonance modes of a confocal prolate metallic nanoshell as a function of the aspect ratio of the core obtained from the static, MLWA, and IMLWA models, respectively. The aspect ratio of the outer surface and foci are fixed at 2/3 and 40 nm, respectively. The nanoshell has a hematite core ($\varepsilon = 9.5$) with the silver shell embedded in the vacuum. The electric field is along the rotational symmetry axis of the spheroidal nanoshell. Note that (a) is in nanometers and (b) is eV for direct comparison with the results in Ref. [8]...39

Figure 4.1 The geometry for the donor (D) and acceptor (A) near the nanorice, with A at various positions oriented normal to the spheroidal surface. 46

Figure 4.2 Comparison of the enhancement factor $R(\omega)$ for different geometries of the nanorice. The foci and the outer (surface) aspect ratio are fixed at 20 nm and 2/3, respectively. The inner aspect ratios are set for three different values, which are 0.2, 0.4, and 0.6. The nanorice has a hematite core ($\varepsilon_1 = 9.5$) with the silver shell embedded in the vacuum. The donor and the acceptor are located at the two “poles” at $(0, 0, 30\,\mathrm{nm})$ and $(0, 0, -30\,\mathrm{nm})$ in Cartesian coordinates and aligned along the z direction. 53

Figure 4.3 Comparison of the enhancement factor $R(\omega)$ for different molecular orientations. The configurations of the nanorice (at a fixed inner aspect ratio of 0.6) and the donor are as in Figure 4.2, but the acceptor is moved to the equatorial position at $(22.36\mathrm{nm}, 0, 0)$ in Cartesian coordinates. Two different orientations are considered with each along the symmetry axis ($\hat{z}$) and perpendicular to the surface (i.e. along $\hat{n}$), respectively. The solid lines indicate the results for the nanorice, where we also show the corresponding results (dashed lines) for a solid spheroid for comparison. 54

Figure 4.4 Comparison of the enhancement factor $R(\omega)$ for different relative positions between the molecules. The configurations of the nanorice (inner aspect ratio 0.4) and the donor are as in Figure 4.2, but the acceptor is varied in position along a spheroidal surface outside the nanorice. The orientations of both the donor and the acceptor are always perpendicular to the surface and the trajectory of the acceptor is fixed on a spheoridal surface with $\xi = 1.5$. 56

Figure 5.1 Two different distributions of the nanoshell composites. (a) The geometry of the nanoshell with inner and outer radius a and b, respectively. The material of core/shell is SiO_2 / Ag with dielectric function $\varepsilon_1 / \varepsilon_2$ 61

Figure 5.2 Temperature dependence of dielectric function of nanoshell composites in MG distribution. The volume fraction is set at $f = 0.01$, and the aspect ratio is set at $a = 30$ nm and $b = 50$ nm 65

Figure 5.3 The imaginary part of the dielectric functions of (a) solid sphere composites and (b) nanoshell composites in MG distribution with different volume fraction f. The temperatures is fixed at 300 K for all plats........66

Figure 5.4 Identical to the Figure 5.3 but with logarithmic scale. 67

Figure 5.5 Fraction dimension dependence of dielectric functions for nanoshell composites in FC distribution with the same parameters as in Figure 5.2. The cluster radius is fixed at $R = 10b$. The temperature is fixed at 300 K. 68

Figure 5.6 Cluster radius dimension dependence of dielectric functions for nanoshell composites in FC distribution with the same parameters as in Figure 5.2. The fractal dimension fixed at $d_f = 2.5$. The temperature is fixed at 300 K...68

Figure 5.7 The temperature dependence of the transmission spectrum for nanoshell composite films in (a) the MG case and (b) the FC case with the same parameters as in Figure 5.2. (c) The transmission of solid sphere composite films in MG and FC cases. The temperature in (c) is fixed at 300 K and the thicknesses of all films are set at $d = 1\,\mu m$ 70

Chapter 1 Introduction

Plasmonics is a new branch of optical science focusing on the collective motion for the free electrons in metallic system [1-3]. Among the many plasmonic systems, metallic nanoparticles play a significant role [4-5]. Because of their high tunibility in the surface plasmon resonance, these resonances depend largely on the geometry and the material response of the nanoparticles.

In the past few years, a very useful nanoparticle in the form of a spheroidal nanoshell was fabricated [6]. The plasmonic properties of this particle are largely dependent on the thickness of the shell, the aspect ratio of the inner and outer radii, and the material response of the core and shell.

Recently, a theoretical model known as “hybridization model” has been introduced to study such a system of spheroidal nanoshell [7-8]. In this hybridization model, the surface charges on both inner and outer interfaces are treated as a free fluid. The whole system is formulated by Lagrangian dynamics. The interaction of these surface charges is accounted for Coulomb potential, thus the results obtain from hybridization model are limited to the electrostatic description [9].

It is well-known as the particle is very small, usually smaller than 1% of the incident wavelength, the electrostatic model can be used as a good approximation[3, 10]. However, for larger particles, the dynamic effects cannot be neglected [5]. This is because the retardation effects will become more and more important as the particle size increases [11-13]. Thus, it is needed to find a new approach which allows us to introduce some of the dynamic effects into these nanoparticle systems. This is one of the main purposes of this thesis.

Our new approach is based on a generalization of the self-consistent effective medium model previously published by Li, Sun, and Chan (LSC) [14]. The main advantage of this new approach is that it allows us to describe a shell particle as an effective solid particle. Hence, one can simply apply the well known results established in the literature for the solid particle to the description of the case of the nanoshell.

We introduce this LSC model in chapter 2, and then apply the so-called modified long-wavelength approximation (MLWA) in LSC model to obtain some of the dynamic effects for the larger nanoshell in chapter 3. In chapter 4, we use the LSC model to study some of the near-field effects focusing on the Förster resonance energy transfer (FRET) between two dipoles in the vicinity of a spheroidal nanoshell. In chapter 5, we study the optical properties of metallic nanoshell composites. Finally, we give a brief summary in the last chapter.

Chapter 2 Polarizability

2.1 Polarizability for a spherical particle

Let us briefly review the definition of polarizability. For a spherical particle with radius a and dielectric function ε embedded in a homogeneous, isotropic and non-absorbing medium with dielectric function ε_h, the electrostatic potential inside and outside the particle can be expressed by

$$\begin{aligned} \psi_{out}(r,\theta,\varphi) &= \sum_{\ell=0}^{\infty}\sum_{m=-\ell}^{\ell}[A_{\ell m}r^{\ell}+B_{\ell m}r^{-\ell-1}]Y_{\ell}^{m}(\theta,\varphi) \\ \psi_{in}(r,\theta,\varphi) &= \sum_{\ell=0}^{\infty}\sum_{m=-\ell}^{\ell}C_{\ell m}r^{\ell}Y_{\ell}^{m}(\theta,\varphi) \end{aligned} \quad . \tag{2.1}$$

Where the coefficient $A_{\ell m}$ indicates the applied field with multipole order (ℓ,m) outside the particle, and $B_{\ell m}$ indicates the corresponding response field due to the induced charge distribution inside the particle. According to the boundary conditions of the electrostatic theory the tangential components of the electric field and the normal components of the displacement field continued at $r=a$, which are

$$\begin{aligned} \psi_{in}(a,\theta,\varphi) &= \psi_{out}(a,\theta,\varphi) \\ -\varepsilon\left.\frac{\partial\psi_{in}(r,\theta,\varphi)}{\partial r}\right|_{r=a} &= -\varepsilon_h\left.\frac{\partial\psi_{out}(r,\theta,\varphi)}{\partial r}\right|_{r=a} \end{aligned} \quad . \tag{2.2}$$

Applying the orthogonal condition of Y_{ℓ}^{m},

$$\int Y_{\ell}^{m}(\theta,\varphi)[Y_{\ell'}^{m'}(\theta,\varphi)]^{*}d\Omega\,, \tag{2.3}$$

the relation between $A_{\ell m}$ and $B_{\ell m}$ can be obtained:

$$B_{\ell m} = -\frac{\ell(\varepsilon - \varepsilon_h)}{\ell\,\varepsilon + (\ell+1)\,\varepsilon} a^{2\ell+1} A_{\ell m} \tag{2.4}$$

This equation indicates the relation between the applied field and the response field. Thus, define the polarizability of the solid sphere as

$$\alpha_{\ell m} \triangleq \frac{\ell(\varepsilon - \varepsilon_h)}{\ell\,\varepsilon + (\ell+1)\,\varepsilon} a^{2\ell+1} \tag{2.5}$$

2.2 Prolate spheroidal coordinates

Now let us consider a more general case: the polarizability for a *spheroidal* particle. Spheroid is a geometrical object made by rotating an ellipse with its major or minor axes. If the rotating axis is major axis, it called prolate spheroid. If the rotating axis is minor axis, it called oblate spheroid, see Figure 2.1. Since the mathematical treatments of these two types of spheroid are quite similar, we only focus on the prolate case.

For a prolate with its two foci locate at $(0,0,f)$ and $(0,0,-f)$ in Cartesian coordinates, see Figure 2.1, can be described by the formula

$$\frac{x^2}{a^2} + \frac{y^2}{a^2} + \frac{z^2}{b^2} = 1\,, \tag{2.6}$$

where a is the semi-minor radius and b is the semi-major radius of the ellipse.

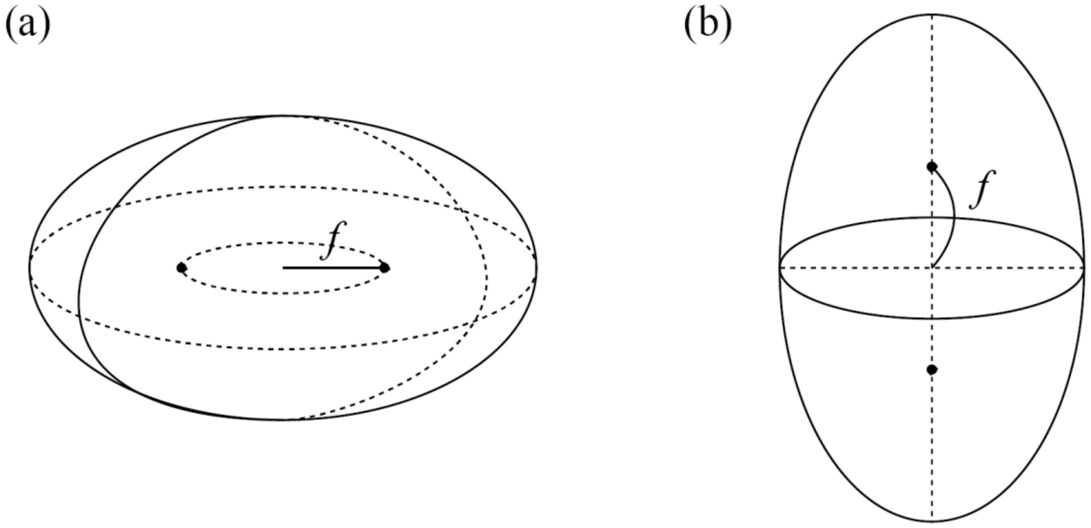

Figure 2.1 Two types of spheroid: (a) oblate and (b) prolate spheroid. f is the focal lengh.

In this prolate spheroid system, it is more convenient to use the prolate spheroidal coordinates: ξ, η and φ [15-16]. For a point (x, y, z) in Cartesian coordinates can be transformed into a prolate spheroidal coordinates (ξ, η, φ) via:

$$\xi = \frac{\rho_1 + \rho_2}{2f}, \qquad \eta = \frac{\rho_1 - \rho_2}{2f}, \qquad \varphi = \arctan\left(\frac{y}{x}\right). \tag{2.7}$$

Where

$$\rho_1 = \sqrt{x^2 + y^2 + (z + f)^2}, \qquad \rho_2 = \sqrt{x^2 + y^2 + (z - f)^2} \tag{2.8}$$

are the distances measured between the point (x, y, z) and the two foci. The value ranges of these three coordinates are $1 \le \xi < \infty$, $1 \le \eta \le -1$, and $0 \le \varphi < 2\pi$. The inverse transformation is

$$\begin{aligned} x &= f\sqrt{(\xi^2-1)(1-\eta^2)}\cos\varphi, \\ y &= f\sqrt{(\xi^2-1)(1-\eta^2)}\sin\varphi, \\ z &= f\,\xi\eta. \end{aligned} \tag{2.9}$$

The Laplace operator in a prolate coordinates is:

$$\begin{aligned} \nabla^2 &= \delta^{ij}\frac{\partial}{\partial x^i}\frac{\partial}{\partial x^j} \\ &= \delta^{ij}\frac{\partial}{\partial x^j}\left(\frac{\partial \xi^k}{\partial x^i}\frac{\partial}{\partial \xi^k}\right) \\ &= \delta^{ij}\frac{\partial \xi^k}{\partial x^i}\frac{\partial \xi^\ell}{\partial x^j}\frac{\partial^2}{\partial \xi^k \partial \xi^\ell} + \delta^{ij}\frac{\partial^2 \xi^k}{\partial x^i \partial x^j}\frac{\partial}{\partial \xi^k} \\ &= \frac{1}{f^2(\xi^2-\eta^2)}\left\{\frac{\partial}{\partial \xi}(\xi^2-1)\frac{\partial}{\partial \xi} + \frac{\partial}{\partial \eta}(1-\eta^2)\frac{\partial}{\partial \eta} + \frac{\xi^2-\eta^2}{(\xi^2-1)(1-\eta^2)}\frac{\partial^2}{\partial \varphi^2}\right\} \end{aligned} \tag{2.10}$$

The Laplace equation, $\nabla^2\psi = 0$, is separable in this prolate spheroidal coordinate system.

We set the general solution of the Laplace equation as:

$$\psi(\xi,\eta,\varphi) = R(\xi)S(\eta)\Phi(\varphi) \tag{2.11}$$

where $R(\xi)$ is called radius function and $S(\eta)$ is called angular function. Substitute into Laplace equation, and then divide by ψ, we have

$$\frac{1}{R(\xi)}\frac{\partial}{\partial \xi}\left[(\xi^2-1)\frac{\partial R(\xi)}{\partial \xi}\right] + \frac{1}{S(\eta)}\left[\frac{\partial}{\partial \eta}(1-\eta^2)\frac{\partial S(\eta)}{\partial \eta}\right] + \frac{\xi^2-\eta^2}{(\xi^2-1)(1-\eta^2)}\frac{1}{\Phi(\varphi)}\frac{\partial^2 \Phi(\varphi)}{\partial \varphi^2} = 0 \tag{2.12}$$

Since φ and $\varphi + 2\pi$ represent the same point in the space, it is naturally to require the constraint:

$$\Phi(\varphi + 2\pi) = \Phi(\varphi) \tag{2.13}$$

In general, we can set

$$\Phi(\varphi) = e^{i\,m\varphi}, \qquad m = 0, \pm 1, \pm 2, \cdots \tag{2.14}$$

Substitute Eq. (2.14) into Eq. (2.12), and rearrange the equation as

$$\frac{1}{R(\xi)}\left[\frac{\partial}{\partial\xi}\left((\xi^2-1)\frac{\partial R(\xi)}{\partial\xi}\right)+\frac{m^2}{\xi^2-1}\right]+\frac{1}{S(\eta)}\left[\frac{\partial}{\partial\eta}\left((1-\eta^2)\frac{\partial S(\eta)}{\partial\eta}\right)+\frac{m^2}{1-\eta^2}\right]=0 \tag{2.15}$$

The first part depends only on ξ, whereas the remainder depends only on η; accordingly, each must be a constant. Now let the separation constant in the form $\ell(\ell+1)$, and then separate Eq. (2.15) into the following two equations:

$$\frac{\partial}{\partial\xi}\left((\xi^2-1)\frac{\partial R(\xi)}{\partial\xi}\right)+\left(\ell(\ell+1)-\frac{m^2}{1-\xi^2}\right)R(\xi)=0 \tag{2.16}$$

$$\frac{\partial}{\partial\eta}\left((\eta^2-1)\frac{\partial S(\eta)}{\partial\eta}\right)+\left(\ell(\ell+1)-\frac{m^2}{1-\eta^2}\right)S(\eta)=0 \tag{2.17}$$

Note that Eqs. (2.16) and (2.17) are the associated Legendre differential equations. Thus, the general solutions of $R(\xi)$ and $S(\eta)$ can be expressed by the linear combination of the first and second kind associated Legendre functions, P_ℓ^m and Q_ℓ^m.

For the angular function, $S(\eta)$, however, $Q_\ell^m(\eta)$ are not convergent solutions of Eq. (2.17) since $Q_\ell^m(\eta)\to\infty$ as $\eta\to 1$. Thus, $P_\ell^m(\eta)$ are the only possible solutions of $S(\eta)$, and it can be expressed as:

$$\begin{aligned} P_\ell^m(\eta) &= \frac{1}{2^\ell\,\ell!}(1-\eta^2)^{m/2}\left(\frac{d}{d\eta}\right)^{\ell+m}(\eta^2-1)^\ell \\ P_\ell^{-m}(\eta) &= (-)^m\frac{(\ell-m)!}{(\ell+m)!}P_\ell^m(\eta) \end{aligned} \tag{2.18}$$

for $m > 0$.

For the radial function, $R(\xi)$, both $P_\ell^m(\xi)$ and $Q_\ell^m(\xi)$ are the possible solutions, which are defined as:

$$P_\ell^m(\xi) = (-i)^m \frac{(\xi^2-1)^{m/2}}{2^\ell \ell!} \left(\frac{d}{d\xi}\right)^{\ell+m} (\xi^2-1)^\ell , \tag{2.19}$$

$$\begin{aligned} Q_\ell^m(\xi) = (-)^m \frac{(\xi^2-1)^{m/2}}{2^\ell \ell!} \left(\frac{d}{d\xi}\right)^m \Bigg\{ & \left(\frac{d}{d\xi}\right)^\ell \left[\ln\left(\frac{\xi+1}{\xi-1}\right) (\xi^2-1)^\ell \right] \\ & -\frac{1}{2} \ln\left(\frac{\xi+1}{\xi-1}\right) \left(\frac{d}{d\xi}\right)^\ell (\xi^2-1)^\ell \Bigg\} \end{aligned} , \tag{2.20}$$

and

$$P_\ell^{-m}(\xi) = (-)^m \frac{(\ell-m)!}{(\ell+m)!} P_\ell^m(\xi) \tag{2.21}$$

$$Q_\ell^{-m}(\xi) = \frac{(\ell-m)!}{(\ell+m)!} Q_\ell^m(\xi) \tag{2.22}$$

for $m > 0$.

Along the positive real axis, the asymptotic properties of the associated Legendre function are [15, 17-18]:

$$\left.\begin{aligned} P_\ell^m(\xi) &\to \frac{(2\ell-1)!!}{(\ell-m)!} i^{-m} \xi^\ell \\ Q_\ell^m(\xi) &\to \frac{(\ell+m)!}{(2\ell+1)!} \xi^{-\ell-1} \end{aligned}\right. \quad \text{for } \xi \to \infty . \tag{2.23}$$

Thus, we can define the normalized function [15]:

$$\begin{aligned} X_\ell^m(\xi, f) &= i^m \frac{(\ell-m)!}{(2\ell-1)!!} f^\ell P_\ell^m(\xi) \\ Z_\ell^m(\xi, f) &= \frac{(2\ell+1)!!}{(\ell+m)!} f^{-\ell-1} Q_\ell^m(\xi) \end{aligned} . \tag{2.24}$$

Then the asymptotic properties of X_ℓ^m and Z_ℓ^m are

$$\begin{aligned} X_\ell^m(\xi, f) &\to (f\xi)^\ell \sim r^\ell \\ Z_\ell^m(\xi, f) &\to (f\xi)^{-\ell-1} \sim r^{-\ell-1} \end{aligned} \quad \text{for } \xi \to \infty . \tag{2.25}$$

where

$$r = \sqrt{x^2+y^2+z^2} = f\sqrt{\xi^2+\eta^2-1} \to f\xi, \qquad \text{for } \xi \to \infty . \tag{2.26}$$

2.3 Polarizability of a prolate spheroidal particle

Consider a prolate spheroidal particle embedded in an uniform medium. The dielectric functions of the particle and the host medium are denoted by ε_1 and ε_2, respectively. The electrostatic potential both inside and outside the spheroid can be expressed as:

$$\begin{aligned} \psi_{in}(\xi,\eta,\varphi) &= \sum_{\ell,m} c_{\ell m} X_\ell^m(\xi, f) Y_\ell^m(\cos^{-1}\eta,\varphi) \\ \psi_{out}(\xi,\eta,\varphi) &= \sum_{\ell,m} [a_{\ell m} Z_\ell^m(\xi, f) + b_{\ell m} X_\ell^m(\xi, f)] Y_\ell^m(\cos^{-1}\eta,\varphi) \end{aligned} . \tag{2.27}$$

Applying the boundary conditions at the interface $\xi = \xi_1$,

$$\psi_{in}(\xi_1,\eta,\varphi) = \psi_{out}(\xi_1,\eta,\varphi) , \tag{2.28}$$

$$\varepsilon_1 \frac{\partial \psi_{in}(\xi,\eta,\varphi)}{\partial \xi}\bigg|_{\xi=\xi_1} = \varepsilon_2 \frac{\partial \psi_{out}(\xi,\eta,\varphi)}{\partial \xi}\bigg|_{\xi=\xi_2} , \tag{2.29}$$

These two equations represent the continuity of the tangential component of the electric fields and the normal component of the electric displacements. Follow these boundary conditions, the relation between $a_{\ell m}$ and $b_{\ell m}$ can be obtained:

$$a_{\ell m} = -(\varepsilon_2 - \varepsilon_1)\left[\varepsilon_2 \left. \frac{\partial Z_\ell^m(\xi, f)/\partial\xi}{\partial X_\ell^m(\xi, f)/\partial\xi} \right|_{\xi\to\xi_1} - \varepsilon_1 \frac{Z_\ell^m(\xi_1, f)}{X_\ell^m(\xi_1, f)} \right]^{-1} b_{\ell m} \tag{2.30}$$

Therefore, the polarizability of the order (ℓ, m) in this case is defined as:

$$\alpha_{\ell m} = f^{2\ell+1} C_{\ell m} \frac{\varepsilon_1 - \varepsilon_2}{\varepsilon_1 A_{\ell m}(\xi_1) - \varepsilon_2 B_{\ell m}(\xi_1)}, \tag{2.31}$$

where

$$A_{\ell m}(\xi) = \frac{Q_\ell^m(\xi)}{P_\ell^m(\xi)}, \qquad B_{\ell m}(\xi) = \frac{[Q_\ell^m(\xi)]'}{[P_\ell^m(\xi)]'}, \qquad C_{\ell m} = i^m \frac{(\ell - m)!(\ell + m)!}{(2\ell - 1)!!(2\ell + 1)!!}. \tag{2.32}$$

2.4 The polarizability of a core-shell particle

The polarizability of a solid sphere and spheroid are described in the previous sections. Now let us consider another situation: a core-shell particle embedded in a medium. In principle the electrostatic potential of the core-shell particle can also be solved by using the similarly method as shown in the previous sections. However, the problem now becomes more complicated since there are two interfaces in the core-shell case. In order to avoid this complicity for solving the boundary value problem we introduce an alternative approach which allows us to replace a single core-shell particle by an equivalent homogeneous particle. This idea comes from Li, Sun, and Chan [14], hence we named this model by “LSC model.”

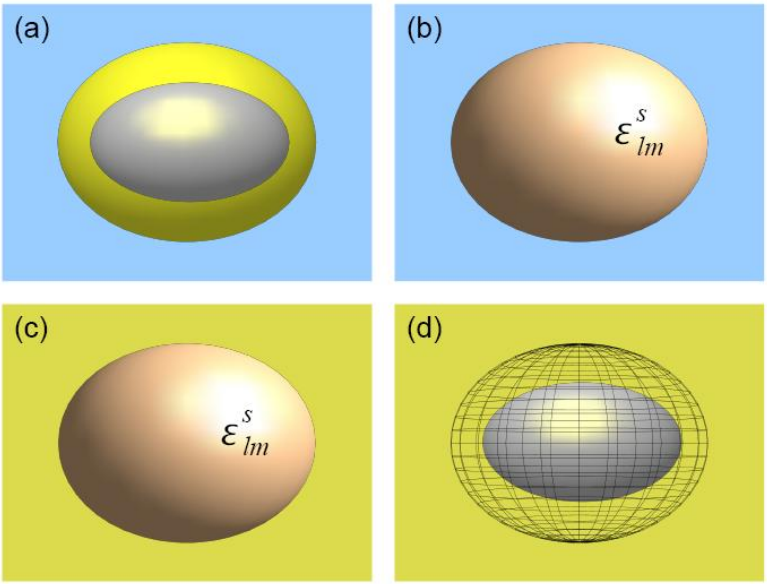

Figure 2.2 Illustration of the approach of the LSC model.

The problem is to drive the multipolar polarizability $\alpha_{\ell m}$ of a single-layer core-shell particle. Figure 2.2 (a) shows a spheroidal core-shell particle embedded in a host medium with a dielectric function ε_h. The dielectric function of the core and the shell are denoted by ε_1 and ε_2, respectively. Our goal is to construct, for each multipole order (ℓ, m), an equivalent solid spheroidal particle with an “effective dielectric function $\varepsilon^{s}_{\ell m}$” and a surface morphology identical to that of the outer surface of the original shell, Figure 2.2 (b), such that its polarizability $\alpha_{\ell m}$ is identical to that of the shell. The key features of the LSC model consist of the following three steps:

(1) Assuming such an “effective spheroidal particle” is found, then we consider the situation when it is hypothetically placed in a medium with a dielectric function ε_2, which is identical to that of the material of the shell, Figure 2.2 (c). For such a case, one can obtain the following expression for the static polarizability of the spheroidal particle form standard solution of the boundary value problem, see Eq. (2.31):

$$\alpha_{\ell m}^{s} = f^{2\ell+1} C_{\ell m} \frac{\varepsilon_{\ell m}^{s} - \varepsilon_2}{\varepsilon_{\ell m}^{s} A_{\ell m}(\xi_2) - \varepsilon_2 B_{\ell m}(\xi_2)}, \tag{2.33}$$

where ξ_2 and f are the spheroidal coordinate indicates the outer surface of the core-shell particle and the foci.

(2) Next, we go back to the original spheroidal shell and consider the case when it is also placed in a medium of dielectric function ε_2, Figure 2.2 (d), rather than in the host medium ε_h. In such a case, it is obvious that the system will simply respond just like a “bare particle” with boundary $\xi = \xi_1$ and dielectric function ε_1. In a similar way as in (1), we then obtain the polarizability of the shell in this case as follows:

$$\alpha_{\ell m}^{1} = f^{2\ell+1} C_{\ell m} \frac{\varepsilon_1 - \varepsilon_2}{\varepsilon_1 A_{\ell m}(\xi_1) - \varepsilon_2 B_{\ell m}(\xi_1)} \tag{2.34}$$

Now if the “effective particle” really represents the original shell, then Eqs. (2.33) and (2.34) must give us identical results when each of them is placed in the same medium of dielectric function ε_2. Here by setting $\alpha_{\ell m}^{s} = \alpha_{\ell m}^{1}$, we can solve for $\alpha_{\ell m}^{s}$ and obtain the following result:

$$\varepsilon_{\ell m}^{s} = \varepsilon_2 \frac{\varepsilon_1[A_{\ell m}(\xi_1) - B_{\ell m}(\xi_2)] - \varepsilon_2[B_{\ell m}(\xi_1) - B_{\ell m}(\xi_2)]}{\varepsilon_1[A_{\ell m}(\xi_1) - A_{\ell m}(\xi_2)] - \varepsilon_2[B_{\ell m}(\xi_1) - A_{\ell m}(\xi_2)]}. \tag{2.35}$$

Note that although Eq. (2.35) is only a necessary condition that the dielectric function $\varepsilon_{\ell m}^{s}$ of the effective particle must fulfill, the uniqueness in the boundary value problem solutions also guarantees it to be a sufficient condition. Hence, Eq. (2.35) implies that one the dielectric and geometric parameters of the original spheroidal shell are given, the effective $\varepsilon_{\ell m}^{s}$ can be uniquely determined.

(3) With the original spheroidal shell now replaced by a solid particle with an effective $\varepsilon_{\ell m}^{s}$ in the same host medium (dielectric constant ε_h), the multipole polarizability of the original shell can then be obtained in the following form [cf. Eq. (2.33) or Eq. (2.34)]:

$$\begin{aligned}\alpha_{\ell m} &= f^{2\ell+1} C_{\ell m} \frac{\varepsilon_{\ell m}^{s} - \varepsilon_h}{\varepsilon_{\ell m}^{s} A_{\ell m}(\xi_2) - \varepsilon_h B_{\ell m}(\xi_2)} \\ &= f^{2\ell+1} C_{\ell m} \frac{(\varepsilon_2 - \varepsilon_h)[\varepsilon_1 A_{\ell m}(\xi_1) - \varepsilon_2 B_{\ell m}(\xi_1)] - (\varepsilon_1 - \varepsilon_2)[\varepsilon_2 B_{\ell m}(\xi_2) - \varepsilon_h A_{\ell m}(\xi_2)]}{[\varepsilon_1 A_{\ell m}(\xi_1) - \varepsilon_2 B_{\ell m}(\xi_1)][\varepsilon_2 A_{\ell m}(\xi_2) - \varepsilon_h B_{\ell m}(\xi_2)] - A_{\ell m}(\xi_2) B_{\ell m}(\xi_2)(\varepsilon_1 - \varepsilon_2)(\varepsilon_2 - \varepsilon_h)}\end{aligned} \tag{2.36}$$

Drude resonance

If one adopts the ideal Drude model for the metallic shell: $\varepsilon_2(\omega) = \varepsilon_2' - \omega_p^2 / \omega^2$, then the resonance frequency of order (ℓ, m) can be obtained from the poles of Eq. (2.36) in the following form:

$$\omega_{\ell m}^{\pm} = \frac{\omega_p}{\sqrt{\varepsilon_2' - \varepsilon_{\ell m}^{\pm}}}, \tag{2.37}$$

with

$$\varepsilon_{\ell m}^{\pm} = \frac{-q_{\ell m} \pm \sqrt{q_{\ell m}^2 - 4p_{\ell m} r_{\ell m}}}{2p_{\ell m}}, \tag{2.38}$$

where

$$p_{\ell m} = A_{\ell m}(\xi_2)[B_{\ell m}(\xi_1) - B_{\ell m}(\xi_2)], \tag{2.39}$$

$$q_{\ell m} = \varepsilon_1 A_{\ell m}(\xi_2)[B_{\ell m}(\xi_2) - A_{\ell m}(\xi_1)] + \varepsilon_h B_{\ell m}(\xi_2)[A_{\ell m}(\xi_2) - B_{\ell m}(\xi_1)], \tag{2.40}$$

and

$$r_{\ell m} = \varepsilon_1 \varepsilon_h B_{\ell m}(\xi_2)[A_{\ell m}(\xi_1) - A_{\ell m}(\xi_2)]. \tag{2.41}$$

Figure 2.3 shows the coupled resonance frequency with two different modes, $m=0$ and $m=1$.

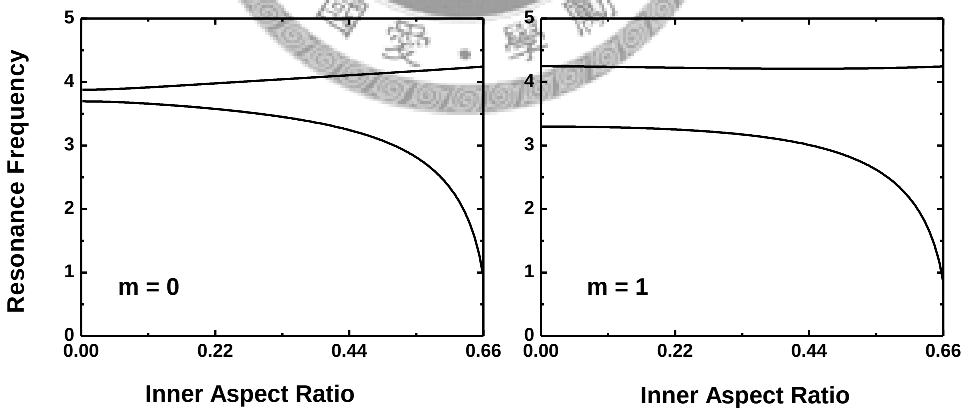

Figure 2.3 Coupled resonance modes, $m=0$ and $m=1$, of a confocal prolate metallic nanoshell as a function of the aspect ratio of the core.

2.5 Dipolar and spherical limits

The dipolar response can be obtained by set $\ell = 1$ in the previous formula. For prolate spheroidal shells, we have the following results,

$$\alpha_{1m} = \frac{f^3}{3} \frac{(\varepsilon_2 - \varepsilon_h)(\varepsilon_1 F_1^m - \varepsilon_2 G_1^m) - (\varepsilon_1 - \varepsilon_2)(\varepsilon_2 G_2^m - \varepsilon_h F_2^m)}{(\varepsilon_1 F_1^m - \varepsilon_2 G_1^m)(\varepsilon_2 F_2^m - \varepsilon_h G_2^m) - (\varepsilon_1 - \varepsilon_2)(\varepsilon_2 - \varepsilon_h) F_2^m G_2^m} \tag{2.42}$$

where

$$F_j^m = \frac{L_m(\xi_j)}{\xi_j(\xi_j{}^2 - 1)}, \qquad G_j^m = \frac{L_m(\xi_j) - 1}{\xi_j(\xi_j{}^2 - 1)}, \qquad j = 1 \text{ or } 2, \qquad m = 0, \pm 1. \tag{2.43}$$

Here (L_0, L_1, L_{-1}) or equivalently (L_x, L_y, L_z) are the static geometrical factors, which are defined as

$$L_0(\xi) = L_z(\xi) = (\xi^2 - 1)\left[\frac{\xi}{2}\ln\left(\frac{\xi + 1}{\xi - 1}\right) - 1\right], \tag{2.44}$$

$$L_{\pm 1}(\xi) = L_x(\xi) = L_y(\xi) = \frac{1 - L_z(\xi)}{2}. \tag{2.45}$$

Note that these factors can also be expressed in a simple form in terms of the eccentricity of the spheroids [11]. Note that the Cartesian components can be obtained from the following relations:

$$\alpha_z = 4\pi\varepsilon_h \alpha_{10}, \qquad \alpha_x = \alpha_y = 4\pi\varepsilon_h \alpha_{11}. \tag{2.46}$$

In the limit of a spherical shell, we consider the parameters $\xi_1 = r_1 / a$, $\xi_2 = r_2 / a$ (with $r_1 < r_2$) and then take the limit $a \to 0$ (hence $\xi_i \to \infty$). Since for $x \to \infty$, we have

$$P_\ell^m(x) \approx \frac{(2\ell-1)!!}{(\ell-m)!} i^{-m} x^{\ell}, \qquad Q_\ell^m(x) \approx \frac{(l+m)!}{(2l+1)!!} x^{-\ell-1} \tag{2.47}$$

we obtain for both the oblate and prolate spheroidal case:

$$A_{\ell m}(\xi) \approx C_{\ell m} \xi^{-2\ell-1}, \qquad B_{\ell m}(\xi) \approx -\frac{\ell+1}{\ell} C_{\ell m} \xi^{-2\ell-1} \tag{2.48}$$

Substitute Eq. (2.48) into Eq. (2.36) yields the following well-known result for a spherical shell [19]:

$$\alpha_{\ell m} = r_2^{\,2\ell+1} \frac{\ell(\varepsilon_2-\varepsilon_h)[\ell\varepsilon_1+(\ell+1)\varepsilon_2] r_1^{2\ell+1} + \ell(\varepsilon_1-\varepsilon_2)[(\ell+1)\varepsilon_2+\ell\varepsilon_h] r_2^{\,2\ell+1}}{[\ell\varepsilon_1+(\ell+1)\varepsilon_2][\ell\varepsilon_2+(\ell+1)\varepsilon_h] r_1^{2\ell+1} + \ell(\ell+1)(\varepsilon_1-\varepsilon_2)(\varepsilon_2-\varepsilon_h) r_2^{\,2\ell+1}} \tag{2.49}$$

which is independent of m.

2.6 Multi-layered spheroidal “nanomatryushka”

For a multi-layered system of confocal spheroidal nanoshells, the LSC model can be applied to two of the shell surfaces at a time starting with the innermost two surfaces. For a system of n-layered shell, the following recurrence relation can be established by generalizing the result in Eq. (2.36):

$$\alpha_{\ell m}^{n} = f^{\,2\ell+1} C_{\ell m} \frac{\left(\varepsilon_n-\varepsilon_h\right)\left(\varepsilon_h \eta_{\ell m}^{n-1} A_{\ell m}^{n-1} - \varepsilon_n \zeta_{\ell m}^{n-1} B_{\ell m}^{n-1}\right) - \left(\varepsilon_h \eta_{\ell m}^{n-1} - \varepsilon_n \zeta_{\ell m}^{n-1}\right)\left(\varepsilon_n B_{\ell m}^{n} - \varepsilon_h A_{\ell m}^{n}\right)}{\left(\varepsilon_n A_{\ell m}^{n} - \varepsilon_h B_{\ell m}^{n}\right)\left(\varepsilon_h \eta_{\ell m}^{n-1} A_{\ell m}^{n-1} - \varepsilon_n \zeta_{\ell m}^{n-1} B_{\ell m}^{n-1}\right) - A_{\ell m}^{n} B_{\ell m}^{n}\left(\varepsilon_h \eta_{\ell m}^{n-1} - \varepsilon_n \zeta_{\ell m}^{n-1}\right)\left(\varepsilon_n - \varepsilon_h\right)} \tag{2.50}$$

where we define

$$\begin{aligned} A_{\ell m}^{n} &= A_{\ell m}(\xi_n), & B_{\ell m}^{n} &= B_{\ell m}(\xi_n) \\ \eta_{\ell m}^{n} &= A_{\ell m}^{n} \alpha_{\ell m}^{n} - C_{\ell m} a^{2\ell+1}, & \zeta_{\ell m}^{n} &= B_{\ell m}^{n} \alpha_{\ell m}^{n} - C_{\ell m} a^{2\ell+1} \end{aligned} \tag{2.51}$$

and the result in Eq. (2.36) is now the value for $\alpha_{\ell m}^2$. Here ξ_n is the n-th boundary of this multi-layered system.

Chapter 3 Dynamic Effects

3.1 Mie theory

In 1908 G. Mie presented a theory describing the scattering and absorption spectra of the spherical particle. It is known as the only exact solution to Maxwell's equations in the problem relative to the particle. Here we briefly review G. Mie's solution which is consider the spherical particle embedded in a uniform medium [10, 20-21]. For a time-harmonic electromagnetic field:

$$\mathbf{E} = \mathbf{E}_0 e^{i(\mathbf{k}\cdot\mathbf{x}-\omega t)}, \quad \mathbf{H} = \mathbf{H}_0 e^{i(\mathbf{k}\cdot\mathbf{x}-\omega t)} \tag{3.1}$$

propagating in a linear, isotropic, homogeneous medium have to satisfy the Maxwell's equations:

$$\begin{aligned} \nabla \cdot \mathbf{E} = 0, \qquad \nabla \times \mathbf{E} = i\omega\mu\mathbf{H} \\ \nabla \cdot \mathbf{H} = 0, \qquad \nabla \times \mathbf{H} = -i\omega\varepsilon\mathbf{E} \end{aligned} \tag{3.2}$$

These four equations may be reduced to the two wave equations:

$$\begin{aligned} \nabla^2 \mathbf{E} + k^2 \mathbf{E} = 0 \\ \nabla^2 \mathbf{H} + k^2 \mathbf{H} = 0 \end{aligned} \tag{3.3}$$

where $k^2 = \omega^2 \varepsilon \mu$.

Now consider a vector function $\mathbf{M} = \nabla \times (\mathbf{c}\psi)$, where $\mathbf{c}$ is a constant vector and ψ is a scalar function. By this definition of $\mathbf{M}$ it is easy to obtain the following relations:

$$\nabla \cdot \mathbf{M} = 0 \tag{3.4}$$

$$\nabla^2 \mathbf{M} + k^2 \mathbf{M} = \nabla \times \left[\mathbf{c} \left(\nabla^2 \psi + k^2 \psi \right) \right] \tag{3.5}$$

Therefore, $\mathbf{M}$ satisfies the wave equation if ψ is also a solution of the wave function:

$$\nabla^2 \psi + k^2 \psi = 0 \tag{3.6}$$

Now define another vector $\mathbf{N}$:

$$\mathbf{N} = k^{-1} \nabla \times \mathbf{M} \tag{3.7}$$

Thus, we have

$$\begin{gathered} \nabla \cdot \mathbf{M} = 0, \quad \nabla \times \mathbf{M} = k\mathbf{N} \\ \nabla \cdot \mathbf{N} = 0, \quad \nabla \times \mathbf{N} = k\mathbf{M} \end{gathered} \tag{3.8}$$

$$\nabla^2 \mathbf{M} + k^2 \mathbf{M} = 0, \quad \nabla^2 \mathbf{N} + k^2 \mathbf{N} = 0 \tag{3.9}$$

This means the properties of $(\mathbf{M}, \mathbf{N})$ are similarly to the electric and magnetic fields $(\mathbf{E}, \mathbf{H})$, compare Eqs. (3.2) and (3.8). Thus, the problem is reduced to solve $(\mathbf{M}, \mathbf{N})$, which only need to find the solution of the scalar wave equation Eq. (3.6). The scalar function ψ is called a generating function for the vector field $\mathbf{M}$ and $\mathbf{N}$; and $\mathbf{c}$ is called the guiding or pilot vector.

In this problem, we take

$$\mathbf{M} = \nabla \times (\mathbf{r}\psi) \tag{3.10}$$

Thus, $\mathbf{M}$ is everywhere tangential to any sphere, i.e., $\mathbf{r} \cdot \mathbf{M} = 0$.

The scalar wave equation in spherical coordinates is

$$\frac{1}{r^2}\frac{\partial}{\partial r}\left(r^2\frac{\partial\psi}{\partial r}\right)+\frac{1}{r^2\sin\theta}\frac{\partial}{\partial\theta}\left(\sin\theta\frac{\partial\psi}{\partial\theta}\right)+\frac{1}{r^2\sin^2\theta}\frac{\partial^2\psi}{\partial\varphi^2}+k^2\psi=0 \tag{3.11}$$

The solutions are

$$\begin{aligned}\psi_{emn}&=\cos m\varphi P_n^m(\cos\theta)z_n(kr)\\ \psi_{omn}&=\sin m\varphi P_n^m(\cos\theta)z_n(kr)\end{aligned} \tag{3.12}$$

where the subscript e and o indicates the even or odd solution, respectively. z_n is any one of the four spherical Bessel functions j_n, y_n, $h_n^{(1)}$, or $h_n^{(2)}$. The vector fields $\mathbf{M}$ and $\mathbf{N}$ are

$$\begin{aligned}\mathbf{M}_{emn}&=\nabla\times(\mathbf{r}\psi_{emn}), & \mathbf{M}_{omn}&=\nabla\times(\mathbf{r}\psi_{omn})\\ \mathbf{N}_{emn}&=k^{-1}\nabla\times\mathbf{M}_{emn}, & \mathbf{N}_{omn}&=k^{-1}\nabla\times\mathbf{M}_{omn}\end{aligned} \tag{3.13}$$

The explicit form may be written:

$$\mathbf{M}_{emn}=\frac{-m}{\sin\theta}\sin m\varphi P_n^m(\cos\theta)z_n(\rho)\hat{\theta}-\cos m\varphi\frac{dP_n^m(\cos\theta)}{d\theta}z_n(\rho)\hat{\varphi} \tag{3.14}$$

$$\mathbf{M}_{omn}=\frac{m}{\sin\theta}\cos m\varphi P_n^m(\cos\theta)z_n(\rho)\hat{\theta}-\sin m\varphi\frac{dP_n^m(\cos\theta)}{d\theta}z_n(\rho)\hat{\varphi} \tag{3.15}$$

$$\begin{aligned}\mathbf{N}_{emn}=&\frac{z_n(\rho)}{\rho}n(n+1)\cos m\varphi P_n^m(\cos\theta)\hat{r}+\cos m\varphi\frac{dP_n^m(\cos\theta)}{d\theta}\frac{1}{\rho}\frac{d}{d\rho}[\rho z_n(\rho)]\hat{\theta}\\ &-m\sin m\varphi\frac{P_n^m(\cos\theta)}{\sin\theta}\frac{1}{\rho}\frac{d}{d\rho}[\rho z_n(\rho)]\hat{\varphi}\end{aligned} \tag{3.16}$$

$$\begin{aligned}\mathbf{N}_{omn}=&\frac{z_n(\rho)}{\rho}n(n+1)\sin m\varphi P_n^m(\cos\theta)\hat{r}+\sin m\varphi\frac{dP_n^m(\cos\theta)}{d\theta}\frac{1}{\rho}\frac{d}{d\rho}[\rho z_n(\rho)]\hat{\theta}\\ &+m\cos m\varphi\frac{P_n^m(\cos\theta)}{\sin\theta}\frac{1}{\rho}\frac{d}{d\rho}[\rho z_n(\rho)]\hat{\varphi}\end{aligned} \tag{3.17}$$

Orthogonal relations

The orthogonal relations of vector fields are given here, one can refer C. F. Bohren's book for more detail [10].

$$\int \mathbf{M}_{em'n'} \cdot \mathbf{M}_{omn} d\Omega = 0, \qquad \forall\ m,\ m',\ n,\ n' \tag{3.18}$$

Similarly, for the pairs $(\mathbf{N}_{omn}, \mathbf{N}_{em'n'})$, $(\mathbf{M}_{omn}, \mathbf{N}_{om'n'})$, $(\mathbf{M}_{emn}, \mathbf{N}_{em'n'})$ are all orthogonal sets for all m, m', n, and n'. Another kind of the orthogonal pairs is for the same type but different order vector fields: $(\mathbf{M}_{emn}, \mathbf{M}_{em'n'})$, $(\mathbf{M}_{omn}, \mathbf{M}_{om'n'})$, $(\mathbf{N}_{emn}, \mathbf{N}_{em'n'})$, and $(\mathbf{N}_{omn}, \mathbf{N}_{om'n'})$ for all $m \neq m'$ or $n \neq n'$.

Spherical harmonic expansion of plane wave

Suppose there is a plane wave incident to a spherical particle with x polarization. The incident wave can be written as

$$\begin{aligned}\mathbf{E}_i &= E_0 e^{ikr\cos\theta}\hat{x} \\ &= \sum_{m=0}^{\infty}\sum_{n=m}^{\infty}(B_{emn}\mathbf{M}_{emn} + B_{omn}\mathbf{M}_{omn} + A_{emn}\mathbf{N}_{emn} + A_{omn}\mathbf{N}_{omn})\end{aligned} \tag{3.19}$$

Apply the orthogonal relations of the vector fields, the incident field can then be written as

$$\mathbf{E}_i = \sum_{n=1}^{\infty} E_n (\mathbf{M}_{o1n}^{(1)} - i\mathbf{N}_{e1n}^{(1)}) \tag{3.20}$$

where $E_n = i^n E_0 (2n+1)/n(n+1)$ and the superscript (1) indicates that $z_n = j_n$. The corresponding incident magnetic field can be obtained by

$$\begin{aligned}\mathbf{H}_i &= -\frac{i}{\omega\mu}\nabla\times\mathbf{E}_i \\ &= \frac{-k}{\omega\mu}\sum_{n=1}^{\infty}E_n(\mathbf{M}_{e1n}^{(1)} + i\,\mathbf{N}_{o1n}^{(1)})\end{aligned} \tag{3.21}$$

Similarly, the field inside the particle can be set as:

$$\begin{aligned}\mathbf{E}_1 &= \sum_{n=1}^{\infty}E_n(c_n\mathbf{M}_{o1n}^{(1)} - i\,d_n\mathbf{N}_{e1n}^{(1)}) \\ \mathbf{H}_1 &= \frac{-k_1}{\omega\mu_1}\sum_{n=1}^{\infty}E_n(d_n\mathbf{M}_{e1n}^{(1)} + i\,c_n\mathbf{N}_{o1n}^{(1)})\end{aligned} \tag{3.22}$$

And also for the scattering field:

$$\begin{aligned}\mathbf{E}_s &= \sum_{n=1}^{\infty}E_n(i\,a_n\mathbf{M}_{e1n}^{(3)} - b_n\mathbf{N}_{o1n}^{(3)}) \\ \mathbf{H}_s &= \frac{k}{\omega\mu}\sum_{n=1}^{\infty}E_n(ib_n\mathbf{N}_{o1n}^{(3)} + a_n\mathbf{N}_{e1n}^{(3)})\end{aligned} \tag{3.23}$$

where the superscript (3) indicates $z_n = h_n^{(1)}$.

Apply the boundary conditions:

$$\begin{aligned}E_{i\theta} + E_{s\theta} &= E_{1\theta}, \qquad E_{i\varphi} + E_{s\varphi} = E_{1\varphi} \\ H_{i\theta} + H_{s\theta} &= H_{1\theta}, \qquad H_{i\varphi} + H_{s\varphi} = H_{1\varphi}\end{aligned} \tag{3.24}$$

One can find the coefficients:

$$a_n = \frac{m\psi_n(mx)\psi_n'(x) - \psi_n(x)\psi_n'(mx)}{m\psi_n(mx)\xi_n'(x) - \xi_n(x)\psi_n'(mx)} \tag{3.25}$$

$$b_n = \frac{\psi_n(mx)\psi_n'(x) - m\psi_n(x)\psi_n'(mx)}{\psi_n(mx)\xi_n'(x) - m\,\xi_n(x)\psi_n'(mx)} \tag{3.26}$$

Where

$$\psi_n(\rho) = \rho j_n(\rho), \qquad \xi_n(\rho) = \rho h_n^{(1)}(\rho) \tag{3.27}$$

Scattering cross sections

The scattered electromagnetic energy crossing an imaginary sphere A outside the particle can be obtained via consider the integration

$$\begin{aligned} W_s &= \int_A \mathbf{S}\cdot d\mathbf{A} \\ &= \frac{1}{2}\mathrm{Re}\int (E_{s\theta}H_{s\varphi}^{*} - E_{s\varphi}H_{s\theta}^{*})d\Omega \\ &= \frac{\pi |E_0|^2}{k\,\omega\,\mu}\sum_{n=1}^{\infty}(2n+1)(|a_n|^2+|b_n|^2) \end{aligned} \tag{3.28}$$

where $\mathbf{S}$ is the poynting vector of the scattered field. The energy of the incident plane wave is

$$\begin{aligned} I_i &= \frac{1}{2}|\mathrm{Re}(\mathbf{E}\times\mathbf{H}^{*})| \\ &= \frac{k}{2\omega\mu}|E_0|^2 \end{aligned} \tag{3.29}$$

Therefore, the scattering cross section is [10]:

$$C_{sca} = \frac{W_s}{I_i} = \frac{2\pi}{k^2}\sum_{n=1}^{\infty}(2n+1)(|a_n|^2+|b_n|^2) \tag{3.30}$$

Similarly, the extinction cross section is:

$$C_{ext} = \frac{W_{ext}}{I_i} = \frac{2\pi}{k^2}\sum_{n=1}^{\infty}(2n+1)\,\mathrm{Re}(a_n+b_n) \tag{3.31}$$

3.2 Modify long wavelength approximation

Although Mie theory is an exact solution of the Maxwell’s equations, however, it is very complicated for the consideration of some other geometrical particle shapes. Thus, there are many other approaches providing a relative simpler method for improving the electrostatic results. Though these methods are not the exact solution of the Maxwell's equations, they give quite precise results for the situation of the particle size small than 10% of the wavelength. Here we give a brief introduction of a model proposed by M. Meier and A. Wokaun in 1983 [11-12].

Consider a sphere embedded in a uniform medium. According to the results of the weak Eshelby conjecture: for any uniform applied field the field inside the particle is uniform if and only if the particle is of elliptic or ellipsoidal in shape [22], the polarization $\mathbf{P}$ inside the particle is uniform and with the relation,

$$4\pi\mathbf{P} = (\varepsilon - 1)(\mathbf{E}_0 + \mathbf{E}_{dip}) \tag{3.32}$$

where $\mathbf{E}_0$ is the external applied field and $\mathbf{E}_{dip}$ is the depolarization field. The depolarization field due to the retarded dipole can be determined by the relation:

$$\begin{aligned} E_r &= 2\cos\theta\left(\frac{[p]}{r^3} + \frac{[\dot{p}]}{cr^2}\right) \\ E_\theta &= \sin\theta\left(\frac{[p]}{r^3} + \frac{[\dot{p}]}{cr^2} + \frac{[\ddot{p}]}{c^2 r}\right) \end{aligned} \tag{3.33}$$

The retarded dipole here is

$$[p] = p e^{ikr}, \qquad [\dot{p}] = -i\omega[p], \qquad [\ddot{p}] = -\omega^2[p] \tag{3.34}$$

Expand e^{ikr} up to the order k^3, and using

$$\begin{aligned} E_{\parallel} &= E_r \cos\theta - E_\theta \sin\theta \\ E_{\perp} &= E_r \sin\theta + E_\theta \cos\theta \end{aligned} \tag{3.35}$$

one can find the depolarization field inside the particle generated by the dipole moment $d\mathbf{p} = \mathbf{P}dV$,

$$dE_{d,\parallel} = \left[\frac{1}{r^3}(3\cos^2\theta - 1) + \frac{k^2}{2r}(\cos^2\theta + 1) + i\frac{2}{3}k^3 \right] PdV \tag{3.36}$$

$$dE_{d,\perp} = \left[\frac{3\sin\theta\cos\theta}{r^3} + \frac{k^2 \sin\theta\cos\theta}{2r} \right] PdV \tag{3.37}$$

For sphere, it is simply to see that $dE_{d,\perp}$ part vanished after integrate over the whole sphere. The result after integrate over the sphere is

$$\mathbf{E}_{dep} = \frac{4\pi}{3}\left(-1 + (ka)^2 + i\frac{2}{3}(ka)^3 \right)\mathbf{P} \tag{3.38}$$

Substitute this result into Eq. (3.32) one have

$$P = \frac{3}{4\pi} \frac{\varepsilon - 1}{(\varepsilon + 2) - (\varepsilon - 1)(ka)^2 - i(2/3)(\varepsilon - 1)(ka)^3} \tag{3.39}$$

The term $-i(2/3)(\varepsilon - 1)(ka)^3$ in the denominator is the radiation-damping correction to the electrostatic solution [23]. The term $-(\varepsilon - 1)(ka)^2$ is the dynamic depolarization which comes from the dynamic effects.

3.3 MLWA for spheroidal nanoshells

Now let us consider this modify long wavelength approximation (MLWA) for the case of nanoshells. Note that the MLWA is the *lowest* order correction which applies only to the modification of the dipolar response [Eqs. (2.42)-(2.46)] and is consistent with the lowest order result from the exact Mie theory [11-12]. In spite of its limitations, the MLWA has been found to be quite accurate for the description of a large range of experiments on these nano particles [5, 24-27].

Note that in the original formalism [11], the MLWA was derived only for the case of a *solid* spherical particle. But since in the LSC model, a spherical shell is now replaced by "an effective solid particle", the MLWA can thus be applied to shell structure as well, as has already been demonstrated in the original LSC paper [14].

Hence, in order to formulate the MLWA for spheroidal shells, we first follow Moroz [11] to express the *static* dipolar (Rayleigh) polarizability of a spheroidal particle in a host (of dielectric constants ε and ε_h, respectively) as follows:

$$\alpha_{1m}^{R} = \frac{V}{4\pi}\frac{\varepsilon-\varepsilon_h}{\varepsilon_h + L_m(\varepsilon-\varepsilon_h)} \tag{3.40}$$

where V is the volume of the particle, and the static geometrical factors L_m are as defined in Eqs. (2.44) and (2.45). Next, as shown by Moroz [11], the MLWA corrections of Meier and Wokaun [12] can be obtained for a spheroid by generalizing Eq. (3.40) to the following form:

$$\begin{aligned}\alpha_{1m}^{MW} &= \frac{\alpha_{1m}^{R}}{1-(D_m/\ell_E)\,k^2\alpha_{1m}^{R} - i\,(2/3)\,k^3\alpha_{1m}^{R}} \\ &= \frac{V}{4\pi}\frac{\varepsilon-\varepsilon_h}{\varepsilon_h + q_m(\varepsilon-\varepsilon_h)}\end{aligned}, \tag{3.41}$$

where ℓ_E is the half-length of the spheroidal axis along which the electric field is applied, and the generalized depolarizing factor q_m which incorporates both geometric and dynamic effects can be expressed as follows:

$$q_m = L_m - \frac{k^2 V}{4\pi \ell_E} D_m - i\frac{2k^3}{3}\frac{V}{4\pi}, \tag{3.42}$$

where D_m is the dynamic geometrical factor as given by Moroz [11], and $k = 2\pi / \lambda$ is the wave vector in free space. Note that while the first term in Eq. (3.42) corresponds to the familiar static polarization term, the second and third terms give rise to the so-called dynamic polarization and radiation reaction which are originated from the exact electrodynamic fields of an oscillating dipole. Hence by using the appropriate quantities $L_m\left(\xi_j\right)$ and $q_m\left(\xi_j\right)$ with $j = 1,2$ corresponding to the inner and outer shells, respectively, into the results expressed in Eqs. (2.42) - (2.46), we can obtain the MLWA results for the polarizability of a spheroidal nanoshell. We give more details for both spheroidal and spherical geometries as follows:

For prolate spheroidal shells:

The dynamic geometrical factors are given by [11]:

$$\begin{aligned} D_0(\xi) = D_z(\xi) &= \frac{3}{4}\left(\frac{\xi^2+1}{\xi^2-1}L_z(\xi)+1\right) \\ D_{\pm 1}(\xi) = D_x(\xi) &= \frac{\sqrt{\xi^2-1}}{2\,\xi}\left(3\xi\,\mathrm{arctanh}\left(\frac{1}{\xi}\right) - D_z(\xi)\right) \end{aligned} \tag{3.43}$$

Hence the MLWA corrections can be obtained by simply replacing F_j^m and G_j^m in Eqs. (2.42) and (2.43) by the following expressions:

$$F_j^m \to \frac{q_m(\xi_j)}{\xi_j(\xi_j^{\,2}-1)}, \quad G_j^m \to \frac{q_m(\xi_j)-1}{\xi_j(\xi_j^{\,2}-1)}, \quad j=1 \text{ or } 2, \quad m=0,\pm 1 \tag{3.44}$$

with q_m given in Eq. (3.42).

Although the above formalism is derived only for a single-layered nanoshell, it is rather straightforward to generalize it to a multi-layered stratified system of spheroidal shells (a “nanomatryushka”) in a systematic way (see Appendix II).

Spherical limit:

By setting $\xi_j = r_j / a$ and let $a \to 0$, we have

$$L_j \to \frac{1}{3}, \quad D_j \to 1, \quad \text{as } \xi \to \infty \tag{3.45}$$

$$q_m(\xi_j) \to q_j = \frac{1}{3} - \frac{1}{3} x_j^{\,2} - i\frac{2}{9} x_j^{\,3} \tag{3.46}$$

where $x_j = k\,r_j = 2\pi r_j / \lambda$, and r_1 and r_2 are the radius of the inner and outer surfaces, respectively. In this limit, we have:

$$F_j^m \to \frac{a^3}{r_j^{\,3}} q_j, \quad G_j^m \to \frac{a^3}{r_j^{\,3}}\left(q_j - 1\right), \quad j=1 \text{ or } 2, \quad m=0,\pm 1 \tag{3.47}$$

With the results in Eqs. (3.45)–(3.47), we finally obtain the following MLWA result for a spherical nanoshell:

$$\alpha_{1m} = \frac{1}{3} r_2^{\,3} \frac{(\varepsilon_2-\varepsilon_h)\left[\varepsilon_1 q_1 - \varepsilon_2(q_1-1)\right] r_2^{\,3} - (\varepsilon_1-\varepsilon_2)\left[\varepsilon_2(q_2-1) - \varepsilon_h q_2\right] r_1^{\,3}}{\left[\varepsilon_1 q_1 - \varepsilon_2(q_1-1)\right]\left[\varepsilon_2 q_2 - \varepsilon_h(q_2-1)\right] r_2^{\,3} - (\varepsilon_1-\varepsilon_2)(\varepsilon_2-\varepsilon_h) q_2(q_2-1) r_1^{\,3}}. \tag{3.48}$$

To our knowledge, the result in Eq. (3.48), being independent of m, has not been obtained before and is as significant as the corresponding one for spherical particles available in the literature [5, 24-27].

3.4 Improvements on MLWA

While the MLWA provides a simple recipe to include the lowest order dynamic corrections to the static polarizability for spheroidal nanoshells as illustrated above, the assumption of uniform polarization inside the particle renders the approach inaccurate for larger size particles. Following Stevenson [28-29] and Moroz [11], we further introduce a semi-empirical "improved MLWA" (IMLWA) which allows the particle polarization along the spheroidal axis of symmetry to vary in magnitude with the angle of inclination (θ) from this axis in the following form:

$$\vec{P} \rightarrow \left(1+\beta k^2 r^2 \sin^2\theta\right)\vec{P}, \tag{3.49}$$

where β is a dimensionless fitting parameter. As a consequence, following Moroz [11], we obtain below a modified dynamic geometrical factor in place of the D_z in Eq. (3.43):

$$D_z = \frac{3}{4\pi a^2}\left[\left(1-2\beta\right)I_0 + \left(1+8\beta\right)I_1 - 6\beta I_2\right] \tag{3.50}$$

where the integrals over the particle volume are defined as:

$$I_n = \int \frac{\cos^{2n}\theta}{2r}\, dV \tag{3.51}$$

For a general spheroidal particle, the integrals in Eq. (3.51) are given in Ref. [11]. For the simple case of a spherical particle, we have $I_n = \dfrac{\pi a^2}{2n+1}$ and $D_z \equiv D = 1 - \dfrac{2}{5}\beta$.

In the following numerical studies, we shall also use this modified dynamic polarization as given in (3.50) and (3.51) to illustrate how good the original MLWA can be improved to, in comparison with the exact electrodynamic results.

3.5 Numerical results

In order to demonstrate the dynamical effects from our MLWA and IMLWA models formulated above for the optical response of a spheroidal nanoshell, we have carried out some numerical studies on the coupled plasmon frequencies and the extinction cross sections of the silver nanoshell systems studied in Ref. [8] within the context of the hybridization model. The dielectric function for silver as given in Ref. [8] has the following form: $\varepsilon(\omega) = \varepsilon_S - \omega_B^2 / \omega(\omega + i\delta)$ with $\varepsilon_S = 5.0$, $\omega_B = 9.5\text{eV}$, and $\delta = 0.15\text{eV}$. To access the accuracy of our various long wavelength approximations, we first compared them with the exact electrodynamic results (Mie theory) for a spherical shell system which are easily available [10].

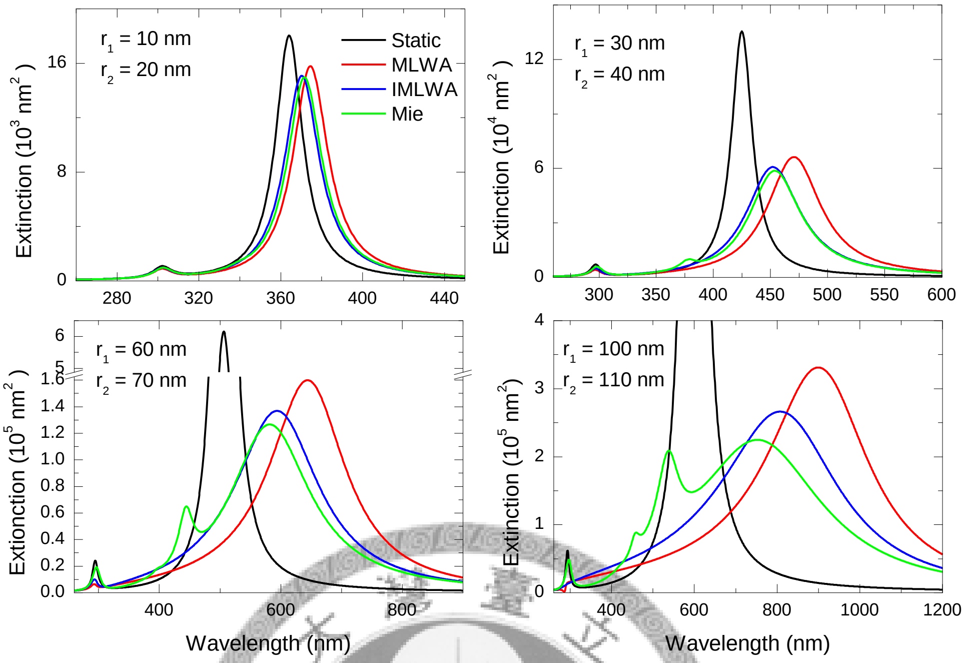

Figure 3.1 Comparison of the extinction cross sections obtained from the static limit, from MLWA, and from IMLWA against the exact Mie theory results. The results are shown for a spherical nanoshell with inner radius r_1 and outer radius r_2 which are shown on the plots. The silver nanoshell is hollow inside and placed in vacuum.

Figure 3.1 shows the calculation of the spectrum of the extinction cross section $\left(\sigma_{ext} = k\,\mathrm{Im}\,\alpha_1\right)$ for a hollow silver spherical shell according to all the three approximations (static, MLWA, and IMLWA with $\beta = 1$) in comparison with the exact electrodynamic result from the Mie theory [10]. As is clear from the figure, while the exact result shows both the split-dipole and the quadrupole modes, all the three approximations can only show the split-dipole modes as expected. Furthermore, while all of them give quite close results for the frequency ω_+ of the antibonding mode, significant errors occur in ω_- with the static model yielding blue-shifted resonances, and the long-wavelength approximations leading to red-shifted resonances for the bonding modes.

Note that it is a rather general result that for a *hollow* shell, the high frequency ω_+ is relatively insensitive to the change in the interaction between the two individual plasmons, and thus retardation effects are quite insignificant for this mode. This is analogous to the in-phase oscillation of two coupled mechanical oscillators with characteristic frequencies quite insensitive to the strength of the coupling. Note also that the blue-shifted peaks from static calculation also occur in a very general way, since retardation effect will lead to an overall weaker interaction between the cavity and the surface plasmons. Most importantly, one sees the significant failure of the static approximation for such a size of the shell $r_1 = 60$ nm and $r_2 = 70$ nm (predicting in this case a blue shift of ~ 20% for ω_- and a peak ~ 5 times larger in value), and how the MLWA (and especially the IMLWA) can yield rather accurate results in comparison with the exact Mie theory. This thus confirms the usefulness of the MLWA's in the calculation of dipole extinction for nanoshells of these dimensions which are often encountered in experimental studies, and are not too small compared to the optical wavelengths used in the experiments.

Having established the accuracy of the MLWA's for spherical nanoshells, we next apply them to the study of speroidal shells. Figure 3.2 shows the calculation of the extinction cross section for the prolate silver spheroidal shell studied in [8] with a dielectric core ($\varepsilon = 9.5$) and foci a =40 nm according to the three models: static, MLWA, and IMLWA. The complete geometry of the nanoshell is specified in the figure caption and the incident plane wave is polarized along the axis of rotational symmetry (note that our above formalism for the IMLWA only applies to this type of polarization). We notice that in this case the high frequency modes are still relatively insensitive to the different models. While the “static results” compare closely to those given by the hybridization model (see Fig. 7 in Ref. [8]), the significance of the corrections from both the long wavelength models is clearly revealed and is qualitatively similar to that found in the case for spherical shells. Again, we expect the result from IMLWA to be closer to the exact one from electrodynamics.

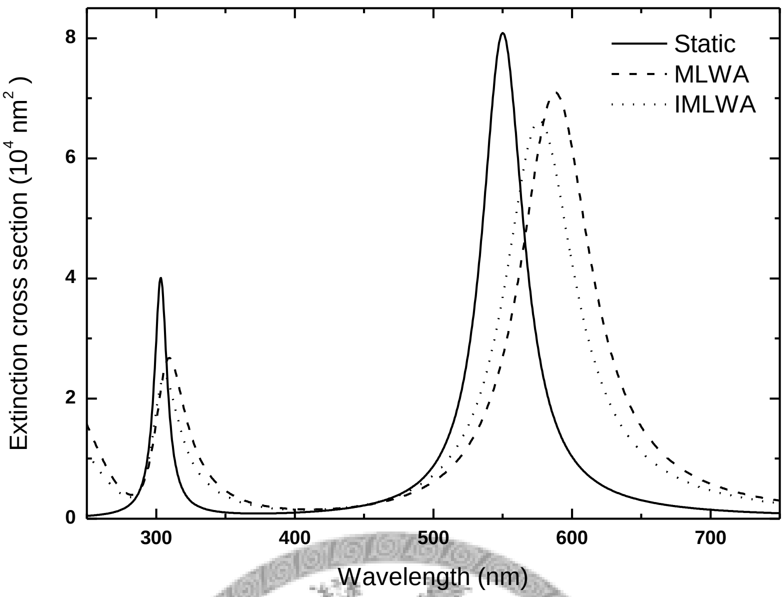

Figure 3.2 Comparison of the extinction cross sections obtained in the static limit, from MLWA, and from IMLWA. The results are shown for a confocal prolate metallic shell with 40 nm foci and aspect ratios 1/2 (core) and 2/3 (outer surface). The nanoshell has a hematite core ($\varepsilon = 9.5$) with the silver shell embedded in vacuum. The electric field is along the rotational symmetry axis of the spheroidal nanoshell.

Having demonstrated the significance of the MLWA's, we next apply it to study the effect of different aspect ratios on the extinction of the nanoshell. Figure 3.3 shows the MLWA results for the spheroidal nanoshell in Figure 3.2 except that now the inner aspect ratio is varied. The polarization of the incident field is along [$m = 0$, Figure 3.3 (a)] and perpendicular [$m = 1$, Figure 3.3 (b)] to the rotational axis, respectively. For the $m = 0$ case, one sees similar qualitative features for the resonance frequencies as observed in the static HM calculation [8] such as the red-shifted bonding mode, and the almost-unchanged antibonding mode with the increase of the inner aspect ratio with fixed outer ratio. However, the values for the cross section obtained in our MLWA are quite different from those obtained in the HM as expected. For the $m=1$ case, Figure 3.3 (b) shows a stronger extinction for the antibonding mode, and the greater dependence of this resonance frequency on the inner aspect ratio, with a blue-shifted peak as the ratio increases. For clarity, we have not shown the IMLWA results in Figure 3.3 (a) but we expect these results will give less red-shifted resonances, and slightly lower peak cross sections compared with those obtained from the MLWA as shown.

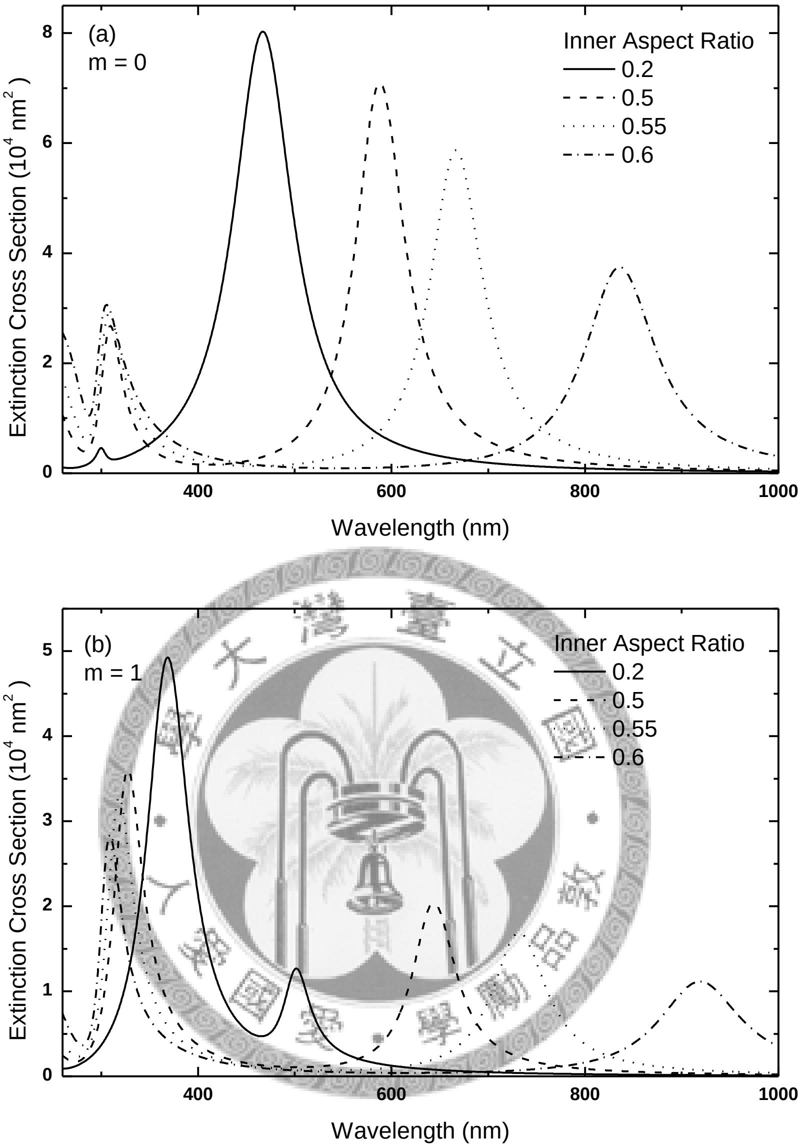

Figure 3.3 The extinction cross section of the confocal prolate metallic nanoshells (foci is fixed at 40 nm) with a fixed aspect ratio (2/3) for the outer surface and four different aspect ratios (0.2, 0.5, 0.55, and 0.6) for the core. The nanoshell has a hematite core ($\varepsilon = 9.5$) with the silver shell embedded in the vacuum. The electric fields are oriented parallel (a) and perpendicular (b) to the rotational symmetry axis of the spheroidal nanoshell. The calculation is based on the MLWA model.

Finally, we also study the split eigen-frequencies using our model. Figure 3.4 shows the resonance frequencies of the coupled bonding and antibonding modes according to the three different models for the same spheroidal shell studied in Fig. 5 of Ref. [8]. We show both the resonance wavelengths [Figure 3.4 (a)] and frequencies in eV [Figure 3.4 (b)] as a function of the inner aspect ratio of the shell. First we point out that our results according to the static model reproduce identical results as obtained from the HM (compare the solid curves in Figure 3.4 (b) to those in Fig. 5 (c) in Ref. [8]). Those obtained from the MLWA's, however, will give red-shifted resonance frequencies in general. These red shifts are particular significant for the bonding modes in the present $m = 0$ case; and we have also found (not shown) that they actually become more pronounced for the antibonding modes in the $m = 1$ case for this filled shell (core with $\varepsilon = 9.5$). In addition, we note that the dynamic modifications are more significant for lower inner aspect ratio of the shell as expected, since the effective scattering volume is greater in this case, which leads to a manifestation of the corrections from the finiteness of the wavelengths within the MLWA approach.

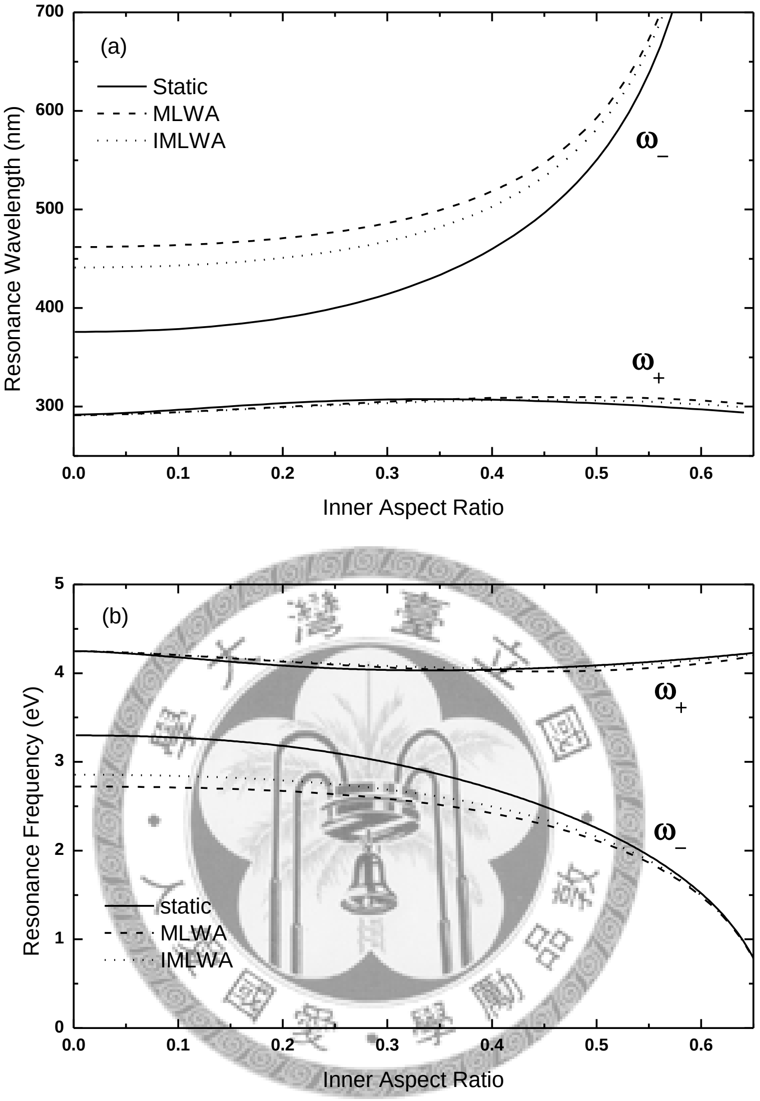

Figure 3.4 coupled resonance modes of a confocal prolate metallic nanoshell as a function of the aspect ratio of the core obtained from the static, MLWA, and IMLWA models, respectively. The aspect ratio of the outer surface and foci are fixed at 2/3 and 40 nm, respectively. The nanoshell has a hematite core ($\varepsilon = 9.5$) with the silver shell embedded in the vacuum. The electric field is along the rotational symmetry axis of the spheroidal nanoshell. Note that (a) is in nanometers and (b) is eV for direct comparison with the results in Ref. [8].

3.6 Discussion and Conclusion

In this chapter, we have presented a systematic formulation, alternative to the hybridization model, for the calculation of the polarizability and coupled resonance frequencies of a spheroidal metallic nanoshell (i.e. nanorice). Our effective medium approach generalizes the previous work (LSC, Ref. [14]) to the spheroidal geometry; which allows for a very efficient computation of the polarizability of the nanoshells, as well as the incorporation of the lowest order dynamic effects in the framework of the MLWA (or IMLWA) for the description of the optical properties of these nanoparticles.

On the other hand, while the hybridization approach is powerful in many aspects in the account of the plasmonic coupling within these nanoshells including the physical origin of the split bonding and antibonding modes; the treatment of very general geometry of interacting surfaces such as two *external* spherical surfaces, two non-concentric surfaces;…etc.; it will be rather nontrivial for it to go beyond the strictly static formulation based on the Coulomb interaction between the uncoupled plasmons, and to account for effects due to the finiteness of the optical wavelengths used in various spectroscopy experiments.

In a wide range of optical experiments involving these metallic nanoshells, it is likely that there is no need for a complicated full electrodynamic analysis of the observations due to the small sizes of these particles in comparison with the wavelengths. Moreover, recent studies have reaffirmed that, the introduction of the lowest order dynamic effects in the form of the MLWA does provide a very good account for many of these experiments – in both far field [5, 24, 26-27] and near field [25] studies. Thus our present work of extending this MLWA (and IMLWA) to spheroidal metallic nanoshells should be of value for future understanding of various optical experiments with these systems of particles of not-too-small sizes (say, for 10 nm < r < 100 nm); especially that our formulation not only yields the coupled resonance frequencies, but also the modified polarizability in a rather straightforward and systematic way. Thus it will be of interest and value to pursue further our present approach, to see if it can also handle other more irregular geometries (e.g. non-concentric shells) so that it can really be established as a viable alternative to the hybridization model for the description of the optical response of these irregular metallic nanoparticles.

Chapter 4 Förster resonance energy transfer

4.1 Introduction

The radiationless energy transfer between a donor molecule (D) and an acceptor molecule (A) at resonance – known as Förster resonance energy transfer (FRET) – is a fundamental process which is significant at close D-A separations (R ~ 2 – 6 nm), and is important for many photophysical and photochemical processes such as photosynthesis [30-31]. It is also a very useful tool as an efficient probe for studying biological systems; and as a rule for various spectroscopic measurements [32]. Moreover, it is a rather weak interaction process based on the electrostatic dipole-dipole interaction between the molecules which falls off in the order of R^{-6}. Hence it will be of great significance if mechanisms can be available through which this weak FRET process can be enhanced to become effective over a greater range with D and A separated over farther distances apart.

Since the first observation of the surface enhanced Raman scattering (SERS) effect in the 1970's and the subsequent recognition of the key role played by the resonant excitation of the collective plasmonic motion of the free electrons in the metallic structure (e.g. on a rough surface) [33], huge amount of effort has been devoted by researchers from different fields to the study of the possibility of plasmonic enhancement for other important optical/spectroscopic processes such as photochemical reactions, spontaneous emission,…etc [34-35]. Not surprisingly, plasmonic enhancement of FRET has also been studied by many people focusing on the interaction between the D and A in the vicinity of certain metallic structure such as a metallic cavity [36], a spherical/spheroidal particle [37-38], a dielectric/metallic cylinder [39], and most recently also metallic nanoshells [40-41]. Experiments have also been successfully carried out in the last few years with single- [42-43] as well as ensemble of molecules[12] confirming the possibility of dramatic plasmonic enhancement of FRET using metallic nanoparticles.

Our present work in this chapter is to explore the possibility of enhancing FRET using one of the most interesting nanoparticle fabricated in the last few years – the metallic nanorice [6]. While the latest theoretical study [39] of RET (both Förster and the far-distance radiative transfer) on an infinite (2D) cylinder has revealed the significance of plasmonic excitations via a comparative study of a dielectric (real constant dielectric function ε) and a metallic cylinder (dispersive and dissipative as described by the Drude-Lorentz model), such phenomenon has also been noted in the literature for some time from the study of FRET at metallic nanoparticles [37-38, 40-41]. In particular, recent studies of FRET at spherical nanoshells have observed greater enhancements for the shell compared to those for a solid particle [41], as well as the importance of higher multipole excitations [40-41]. Furthermore, the significance of the bonding and antibonding modes from the coupling ("hybridization") of the surface and cavity modes, as well as the nonlocal optical response of the metallic shell have also been established [40]. However, while the spherical nanoshells admit high tunability in their bonding and antibonding modes via the adjustment of the size and thickness of the shell, the recently-fabricated (spheroidal) nanorice will be in addition capable of providing much greater enhanced local fields for the FRET process. Furthermore, it may have even higher tunability due to the greater number of geometric parameters (e.g. the aspect ratio) available for adjustment. Hence it will be of interest to calculate the FRET rate at such a nanorice to provide guidance for possible future experimental observations.

4.2 Theoretical model

In our present formulation, we shall model the D and A as harmonic point dipoles interacting directly with each other, as well as via the electromagnetic interaction mediated by a spheroidal metallic nanorice (Figure 4.1).

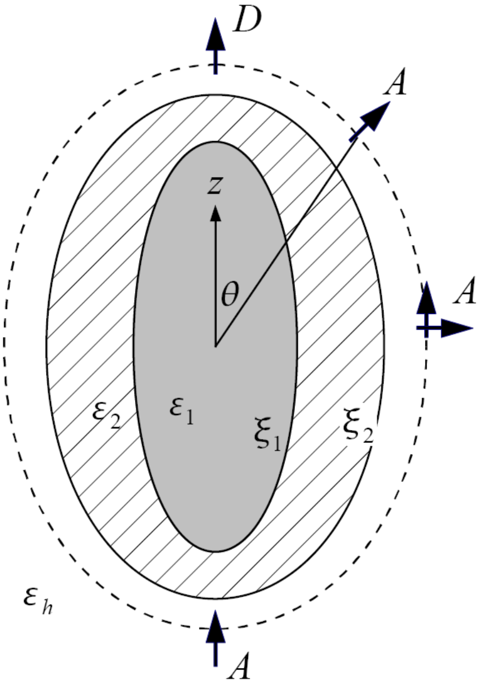

Figure 4.1 The geometry for the donor (D) and acceptor (A) near the nanorice, with A at various positions oriented normal to the spheroidal surface.

To calculate the FRET rate (K) between the D and the A, we follow the original theory [30-31, 38] which applied the Fermi golden rule and obtain the following expression:

$$K(\omega) = \frac{9c^4}{8\pi}\frac{\sigma_A(\omega)\Gamma_D(\omega)}{\omega^4}\,|\,U(\omega)\,|^2, \tag{4.1}$$

where $\sigma_A(\omega)$ is the absorption cross section of the acceptor, $\Gamma_D(\omega)$ the emission rate per unit frequency of the donor, and $U(\omega)$ is the interaction energy between D and A in the presence of the nanorice. In principle, both the absorption and emission of the molecules will be modified by the presence of the nanorice. However, as discussed previously [40], these modifications are of higher order effects. Hence, to first order perturbation, the presence of the nanorice will only modify $U(\omega)$ which we shall study in the following adopting the long wavelength (electrostatic) approximation.

FRET on a spheroidal solid particle

Before we consider the nanorice case, let us first review briefly the problem of energy transfer between the D and A near a solid spheroidal particle [38]. Working in spheroidal coordinates (ξ, η, φ), the electrostatic potential both inside and outside the particle can be obtained by solving the Laplace equation $\nabla^2 \Phi = 0$ [38]. For a position outside the particle ($\xi > \xi_2$), the potential can be expressed as

$$\tilde{\Phi}(\mathbf{r}) = \Phi_D(\mathbf{r}) + \tilde{\Phi}_{D,ind}(\mathbf{r}) + \Phi_A(\mathbf{r}) + \tilde{\Phi}_{A,ind}(\mathbf{r}), \tag{4.2}$$

where

$$\Phi_J(\mathbf{r}) = \frac{\boldsymbol{\mu}_J \cdot (\mathbf{r} - \mathbf{r}_J)}{|\mathbf{r} - \mathbf{r}_J|^3}, \quad J = D, A \tag{4.3}$$

is the dipolar potential associated with the isolated donor (D) or acceptor (A), and

$$\tilde{\Phi}_{J,ind}(\mathbf{r}) = -\boldsymbol{\mu}_J \cdot \sum_{n=0}^{\infty} \sum_{m=0}^{n} \frac{\tilde{\alpha}_{nm}}{f} \nabla_J [Q_n^m(\xi_J) Q_n^m(\xi) P_n^m(\eta_J) P_n^m(\eta) \cos m(\varphi_J - \varphi)], \quad J = D, A \tag{4.4}$$

is the potential due to the induced charge (on the particle) caused by the donor or acceptor, where P_n^m and Q_n^m are the associated Legendre functions, and f is the foci of the prolate spheroid. Here we shall use the symbol tilde (~) for quantities in the case of solid particle to distinguish from those for the nanorice. The quantity $\tilde{\alpha}_{nm}$ in Eq. (4.4) can be obtained as [38]

$$\tilde{\alpha}_{nm} = F_{nm} \frac{\varepsilon - \varepsilon_h}{\varepsilon A_{nm}(\xi_2) - \varepsilon_h B_{nm}(\xi_2)}, \tag{4.5}$$

which is a dimensionless factor determined by the geometry and the dielectric property of the particle (ε) and that of the host medium (ε_h). The various coefficients in Eq. (4.5) are defined as follows:

$$A_{nm}(\xi) = \frac{Q_n^m(\xi)}{P_n^m(\xi)}, \quad B_{nm}(\xi) = \frac{[Q_n^m(\xi)]'}{[P_n^m(\xi)]'}, \quad F_{nm} = (-1)^m (2 - \delta_{m,0})(2n+1)\left[\frac{(n-m)!}{(n+m)!}\right]^2, \tag{4.6}$$

where $(')$ denotes the derivative with respect to the argument as indicated.

FRET on a spheroidal nanoshell

Next we consider the energy transfer process between the D and A in the vicinity of a nanorice modeled as a confocal prolate spheroidal nanoshell (Figure 4.1), where the two interfaces are specified by $\xi = \xi_1$ and $\xi = \xi_2$ in prolate spheroidal coordinates, with the same foci for these interfaces [8]. It is clear that a direct approach to solving the boundary value problem for this case will be very involved. However, in chapter 2 or Ref. [9], we have discovered that an application of a previously-formulated effective medium model [14] can greatly simplify the mathematical description of the dielectric response of a spheroidal nanoshell, and it is this approach we shall apply in our following study of the FRET process at a nanorice.

The main idea of this effective medium model is to replace the multilayer shell structure of different media by a homogeneous *solid* particle (i.e. a solid spheroid) with an *effective* dielectric function accounting for *both* the geometric and dielectric characteristics of the given shell. By requiring this "effective particle" with the shape of the external surface (dimension ξ_2) to produce the *same* multipolar polarizability of the original spheroidal shell, in an environment when the outside medium is filled with the material of the shell (dielectric function ε_2) [9, 14], the effective dielectric function can be obtained as:

$$\varepsilon_{nm}^{s}=\varepsilon_2\frac{\varepsilon_1\left[A_{nm}\left(\xi_1\right)-B_{nm}\left(\xi_2\right)\right]-\varepsilon_2\left[B_{nm}\left(\xi_1\right)-B_{nm}\left(\xi_2\right)\right]}{\varepsilon_1\left[A_{nm}\left(\xi_1\right)-A_{nm}\left(\xi_2\right)\right]-\varepsilon_2\left[B_{nm}\left(\xi_1\right)-A_{nm}\left(\xi_2\right)\right]}. \tag{4.7}$$

Using this result, the potential of the D-A system outside the spheroidal shell (Figure 4.1) can simply be obtained from the results in Eqs. (4.2)-(4.6) by replacing the dielectric function ε by ε_{nm}^{s} for each multipole order (n,m). Thus we have (all quantities without tilde):

$$\Phi(\mathbf{r})=\Phi_D(\mathbf{r})+\Phi_{D,ind}(\mathbf{r})+\Phi_A(\mathbf{r})+\Phi_{A,ind}(\mathbf{r}), \tag{4.8}$$

where

$$\Phi_{J,ind}(\mathbf{r})=-\boldsymbol{\mu}_J\cdot\sum_{n=0}^{\infty}\sum_{m=0}^{n}\frac{\alpha_{nm}}{f}\nabla_J[Q_n^m(\xi_J)Q_n^m(\xi)P_n^m(\eta_J)P_n^m(\eta)\cos m(\varphi_J-\varphi)],\quad J=D,\,A \tag{4.9}$$

and [9]

$$\alpha_{nm} = F_{nm} \frac{(\varepsilon_2 - \varepsilon_h)[\varepsilon_1 A_{nm}(\xi_1) - \varepsilon_2 B_{nm}(\xi_1)] - (\varepsilon_1 - \varepsilon_2)[\varepsilon_2 B_{nm}(\xi_2) - \varepsilon_h A_{nm}(\xi_2)]}{[\varepsilon_1 A_{nm}(\xi_1) - \varepsilon_2 B_{nm}(\xi_1)][\varepsilon_2 A_{nm}(\xi_2) - \varepsilon_h B_{nm}(\xi_2)] - A_{nm}(\xi_2) B_{nm}(\xi_2)(\varepsilon_1 - \varepsilon_2)(\varepsilon_2 - \varepsilon_h)}$$

(4.10)

where we have made explicit use of the result in Eq. (4.7).

The electric field $\mathbf{E}_A$ at the acceptor position can then be obtained from the expression

$$\mathbf{E}_A = -\nabla[\Phi_D(\mathbf{r}) + \Phi_{D,ind}(\mathbf{r}) + \Phi_{A,ind}(\mathbf{r})]\Big|_{\mathbf{r}=\mathbf{r}_A} . \qquad (4.11)$$

Hence the interaction energy for the acceptor in the presence of both the donor and the nanorice is obtained as:

$$\begin{aligned} U_A &= -\boldsymbol{\mu}_A \cdot \mathbf{E}_A \\ &= U_{AD} + U_{AD,ind} + U_{AA,ind} \end{aligned}, \qquad (4.12)$$

where

$$U_{A,D} = \frac{\boldsymbol{\mu}_A \cdot \boldsymbol{\mu}_D}{|\mathbf{r}_A - \mathbf{r}_D|^3} - \frac{3\boldsymbol{\mu}_A \cdot (\mathbf{r}_A - \mathbf{r}_D)\boldsymbol{\mu}_D \cdot (\mathbf{r}_A - \mathbf{r}_D)}{|\mathbf{r}_A - \mathbf{r}_D|^5} , \qquad (4.13)$$

and

$$U_{IJ,ind} = -\sum_{n=0}^{\infty}\sum_{m=0}^{n} \frac{\alpha_{nm}}{f} (\boldsymbol{\mu}_I \cdot \nabla_I)(\boldsymbol{\mu}_J \cdot \nabla_J)[Q_n^m(\xi_I) Q_n^m(\xi_J) P_n^m(\eta_I) P_n^m(\eta_J) \cos m(\varphi_I - \varphi_J)]$$
$$I, J = D \text{ or } A$$

(4.14)

To study the energy transfer between the donor and acceptor we only have to consider the first two terms in Eq. (4.12), i.e. $U_{AD} + U_{AD,ind}$ with the latter given as in Eq. (4.14). The last term in (4.12), $U_{AA,ind}$, is associated with the energy transfer between the acceptor and the nanorice which leads to modifications on the decay rates of the acceptor molecule [38]. From this and the result in Eq. (4.1), we can now introduce the enhancement factor for the FRET process at a nanorice defined as:

$$R = \left| \frac{U_{AD} + U_{AD,ind}}{U_{AD}} \right|^2 = \left| 1 + \frac{U_{AD,ind}}{U_{AD}} \right|^2, \tag{4.15}$$

which measures the efficiency of the energy transfer between the D and A in the vicinity of the nanorice.

4.3 Numerical results

For all computations in this section, the nanorice is made by a dielectric core (hermatite, $\varepsilon_1 = 9.5$) covered by a silver shell and embedded in the vacuum [8]. The semi-major and semi-minor axes of the outer surface are fixed at 26.8 nm and 17.9 nm, respectively, and the dielectric function of silver is described by the following Drude model [8]:

$$\varepsilon_2(\omega) = \varepsilon_s - \frac{\omega_p^2}{\omega(\omega + i\delta)}, \tag{4.16}$$

with $\varepsilon_s = 5$, $\omega_p = 9.5\ \mathrm{eV}$, and $\delta = 0.15\ \mathrm{eV}$. We divide our numerical studies of the enhancement spectrum into the following three aspects:

a. Effects from the nanoshell geometry

Here we fix the outer shell geometry along with the positions and orientations of the two molecules D and A (see caption of Figure 4.2), but with the inner aspect ratio varied. As this ratio increases, the thickness of the silver shell decreases and one would expect cross-coupling of the plasmons at the two interfaces will become more significant. Indeed, from the results of Figure 4.2, one can clearly draw the following conclusions: (i) as in the spherical case [40], all the shell structures (in contrast to the solid spheroid case) yield resonances split into the low frequency bonding and high frequency antibonding modes, with the splitting more pronounced as the shell gets thinner; (ii) enhancements from the bonding modes are in general greater (up to an order of magnitude) than the corresponding ones from the antibonding models, due to the relative dominance of the outer surface modes over the cavity modes; and (iii) multipolar resonances emerge and can be resolved mostly for the bonding modes except for the thinnest case (aspect ratio 0.6) where they can also be seen among the antibonding modes. All these results are in qualitative consistence with those observed previously for a spherical nanoshell [40].

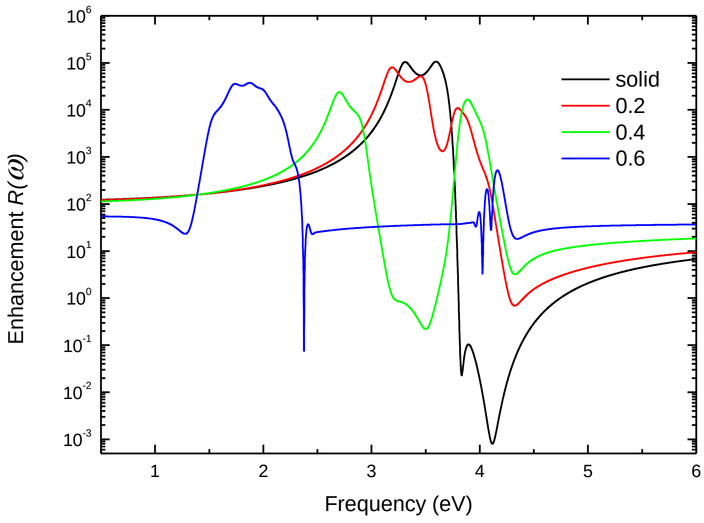

Figure 4.2 Comparison of the enhancement factor $R(\omega)$ for different geometries of the nanorice. The foci and the outer (surface) aspect ratio are fixed at 20 nm and 2/3, respectively. The inner aspect ratios are set for three different values, which are 0.2, 0.4, and 0.6. The nanorice has a hematite core ($\varepsilon_1 = 9.5$) with the silver shell embedded in the vacuum. The donor and the acceptor are located at the two "poles" at $(0, 0, 30\,\text{nm})$ and $(0, 0, -30\,\text{nm})$ in Cartesian coordinates and aligned along the z direction.

b. Effects from the orientations of the molecules

In this case, we have the donor fixed at the north pole as in Figure 4.2, but the acceptor moved to the equatorial position at which two orthogonal orientations (i.e., the normal $\hat{n}$ and tangential $\hat{z}$ orientations) of it are considered. From the enhancement spectrum in Figure 4.3, we observe that while the multipolar feature in the solid particle case differs appreciably for the two molecular orientations; that for the two split resonances in the nanorice case is less pronounce with both the $\hat{n}$ and $\hat{z}$ oriented acceptor yielding rather similar resonance structure. Since here we consider a rather thin shell (with aspect ratio fixed at 0.6), we observe the multipolar resonance for both the bonding and antibonding modes as revealed in Figure 4.2. The most interesting observation from Figure 4.3 is the general greater enhancement obtained in the case with the D and A in a relatively perpendicular orientation (i.e. A along $\hat{n}$ in this case). This is generally valid for both the solid and shell particles, except for frequencies close to the plasmon resonances, and can be understood from the electrostatic interaction between two arbitrarily oriented dipoles.

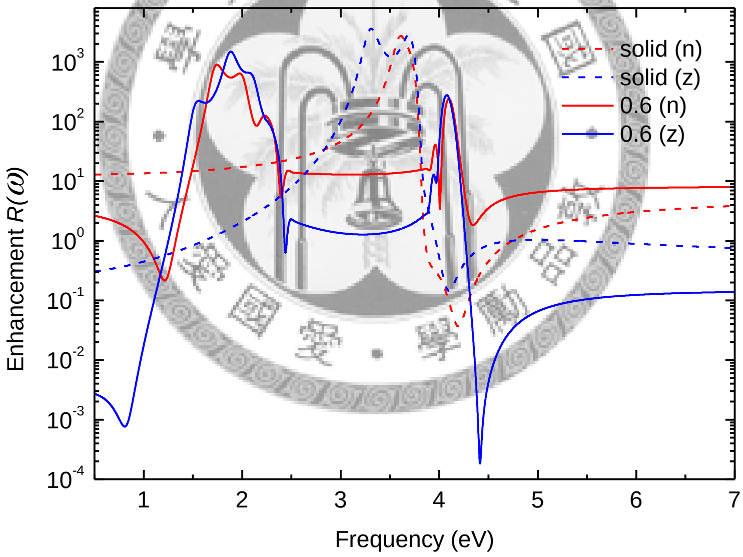

Figure 4.3 Comparison of the enhancement factor $R(\omega)$ for different molecular orientations. The configurations of the nanorice (at a fixed inner aspect ratio of 0.6) and the donor are as in Figure 4.2, but the acceptor is moved to the equatorial position at $(22.36\text{nm}, 0, 0)$ in Cartesian coordinates. Two different orientations are considered with each along the symmetry axis ($\hat{z}$) and perpendicular to the surface (i.e. along $\hat{n}$), respectively. The solid lines indicate the results for the nanorice, where we also show the corresponding results (dashed lines) for a solid spheroid for comparison.

c. Effects from the relative positions of the molecules

Finally we study the enhancement as a function of the relative position between the D and A. Here we have D fixed at the north pole and the position of A varied along a spheroidal surface with ξ=1.5. The orientations of both molecules are all the time in the normal direction. Positions of A at various angles from the positive z axis are studied as indicated in Figure 4.4, from which one observed that the values of the two resonance frequencies remain roughly unchanged for all the angular positions of A since they are determined largely by the geometry and materials of the nanoshell which remain constant throughout. However, it is worthwhile to note that the enhancement ratio increases as A and D get farther from each other due to the decrease in the strength in the direct transfer between them.

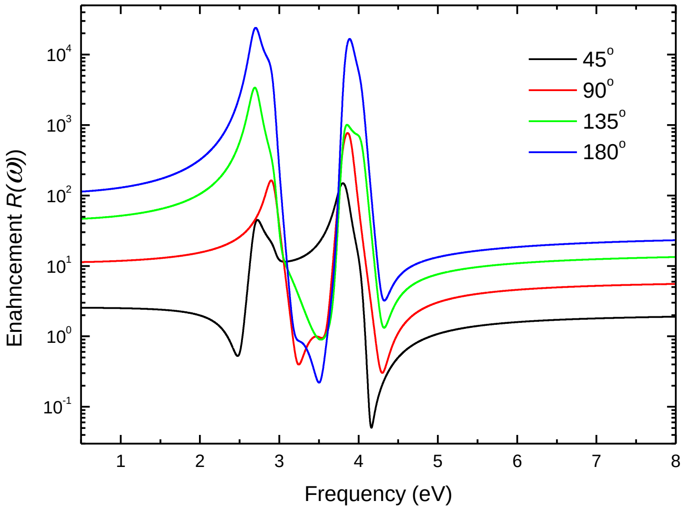

Figure 4.4 Comparison of the enhancement factor $R(\omega)$ for different relative positions between the molecules. The configurations of the nanorice (inner aspect ratio 0.4) and the donor are as in Figure 4.2, but the acceptor is varied in position along a spheroidal surface outside the nanorice. The orientations of both the donor and the acceptor are always perpendicular to the surface and the trajectory of the acceptor is fixed on a spheoridal surface with $\xi = 1.5$.

4.4 Conclusion

In this chapter we have presented some model studies of the FRET process between two molecules in the vicinity of a metal nanorice, generalizing the previous works on metallic spheroidal particles [38] and spherical nanoshells [41-43]. Numerical results show that while FRET enhancements at spheroidal shells are comparable to the corresponding ones for solid spheroids, the plasmonic tunability into the bonding and antibonding resonance modes is much higher in the shell case. In addition, interesting dependence of the enhanced FRET on the relative orientation and position of the two molecules is observed.

Our approach is based on a effective medium theory [9, 14] which highly simplified the multi-boundary value problem of the spheroidal shell structure. Though we have so far only studied cases with *both* the molecules lying outside the nanoshell, it is possible to employ the present formalism to study also cases with one or both the molecules lying within the structure, as was done in our previous study [40]. In addition, we also have not studied the possible nonlocal optical response from the nanorice as we have done for the spherical shells [40]. Note also that even within the context of our previous effective medium model [9], here we cannot incorporate the modified long-wavelength approximation (MLWA) formulated there to improve our purely-electrostatic calculations, since this was formulated only for dipolar response whereas here we need to account for many higher-order multipoles in our study of near-field interactions for the FRET process. Thus it is clear that while our present modeling results should be of interest for future experiments to compare with; there are also rooms for future improvements in the theoretical modeling of the phenomenon --- one which is highly significant in many photophysical processes in Nature.

Chapter 5 Metallic Nanoshell Composites

5.1 Introduction

Since its first fabrication in 1998 [44], the spherical metallic nanoshell has evolved to become one of the most versatile plasmonic systems with significant potential applications from spectroscopic enhancements to cancer therapy [45-46]. Due to its high flexibility in the variations of the core and shell materials as well as in the aspect ratio, it possesses high tunability in its plasmonic resonances covering the whole visible range and beyond. This has hence motivated a large number of studies in the past decade on the fundamental optical properties of this system, both in experiment and in theory [45-46]. Moreover, in applications, both individual nanoshells and composites made of these shells are of significance; and it seems that the study of the optical properties of the latter has started to receive attentions from researchers only in the last few years [14, 47-49].

It is the purpose of our present study in this chapter to report new observations from theoretical modeling on the optical behaviors of some of these composites which contain a collection of these nanoshells, dispersed randomly in the form of either isolated particles or in clustered state throughout an insulating solid host. This mimics a kind of “nanoshell cermets” and is different from the recently-studied photonic crystals composed of such shells [14, 47]. The ellipsoidal shell composite studied in [48-49] is similar to ours, and the focus there has been on the effects from the particle shape distribution in the composite. Our focus here, however, will be on the effects from particle-clustering of these shells, as well as from temperature variations on the optical properties of these composites which the previous works have not studied [48-49]. One motivation for the study of the temperature effects is from the recent proposition of drug-delivery applications via manipulations of these effects [50]. In addition, temperature dependent optical bistability has been reported for composites of nanoshells made of metallic core coated with nonlinear dielectric [51]. Previously, we have studied these temperature effects on the optical properties of individual isolated nanoshells in their function as spectroscopic enhancers [52-53]. We shall employ the same temperature model for our present study of the composite; and as for the particle-clustering phenomenon, we shall assume fractal-clusters are formed in the composite and employ the previously-available effective medium models in the literature. For simplicity, we shall only consider spherical nanoshells in the present study.

5.2 Theoretical model

For a system of metallic nanoshells in a solid dielectric host with the shells distributed randomly either in isolated or in clustered form throughout the host as illustrated with various parameters specified in Figure 5.1, let us first recapitulate the essence of several models from previous literature which will be useful for our numerical studies in the present work.

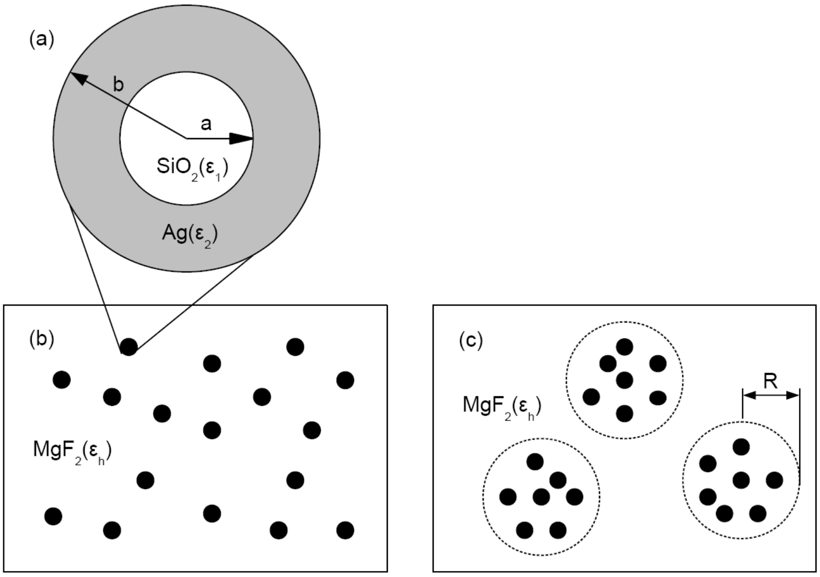

Figure 5.1 Two different distributions of the nanoshell composites. (a) The geometry of the nanoshell with inner and outer radius a and b, respectively. The material of core/shell is SiO_2 / Ag with dielectric function $\varepsilon_1 / \varepsilon_2$.

a. EMT for randomly-distributed nanoshells

According to the results of chapter 2, an individual nanoshell can be replaced by an effective spherical particle of the same size, see Eq. (2.35). For the spherical limitation Eq.

(2.35) reduce to

$$\varepsilon_s = \varepsilon_2 \frac{\varepsilon_1(b^3 + 2a^3) + 2\varepsilon_2(b^3 - a^3)}{\varepsilon_1(b^3 - a^3) + \varepsilon_2(2b^3 + a^3)} \tag{5.1}$$

Now we can apply the well-established effective medium theory (EMT) to obtain the dielectric response of the composite. For the case when the particles disperse randomly throughout the host (of dielectric constant ε_h), we have here the effective dielectric function $\bar{\varepsilon}$ given simply by the Maxwell-Garnett (MG) model in the form [54-55]:

$$\frac{\varepsilon_s + 2\varepsilon_h}{\varepsilon_s - \varepsilon_h} = f \frac{\bar{\varepsilon} + 2\varepsilon_h}{\bar{\varepsilon} - \varepsilon_h} \tag{5.2}$$

where f is the volume fraction of the particles.

b. EMT for clustered nanoshells

For the case when the particles coalesce to form fractal-clusters (FC) in the host, we apply the differential-effective medium model available in the literature [56] and obtain the average dielectric function $\varepsilon(R)$ for a spherical FC of radius R, in the limit of low particle concentration given implicitly by the following cubic equation:

$$\frac{\varepsilon(R)}{\varepsilon_S(b)} \left[\frac{\varepsilon_h - \varepsilon_S(b)}{\varepsilon_h - \varepsilon(R)} \right]^3 = f' \tag{5.3}$$

where $f' = \left[\frac{R}{b} \right]^{3(3-d_f)}$ is the volume fraction of the particles *in the cluster* with d_f the fractal dimension of the cluster. Note that we have explicitly stated the size of the effective particle (radius b) in Eq. (5.3). The dielectric function of the composite in this case will be obtained by applying the MG theory once more to a system with the same host but containing a randomly distributed collection of these “clustered particles” of radius R and dielectric constant $\varepsilon(R)$ obtained from solving Eq. (5.3). In addition, the concentration of these “clustered particles” will be given by a volume fraction $f_C = f \cdot (f')^{1/3}$, where f is the original given volume fraction of nanoshells in the composite. Hence using Eq. (5.2) with $\varepsilon_S \to \varepsilon(R)$ and $f \to f_C$, we can finally obtain the effective dielectric function for the whole composite with the nanoshells forming fractal clusters in the host dielectric.

c. Model for temperature effects

To account for the temperature effects on the optical properties of these nanoshell composites, we assume such effects are only significant for the metallic part of the shell and describe its dielectric response using the Drude model:

$$\varepsilon = 1 - \frac{\omega_P^2}{\omega\left(\omega + i\omega_c\right)} \tag{5.4}$$

where $\omega_C(T)$ is the collision frequency and $\omega_P(T)$ the plasma frequency, whose temperature dependence can be found from our previous work [52]. The collision frequency will have contributions from both phonon-electron and electron-electron scattering, as well as a surface scattering term from the two shell boundaries [52]:

$$\omega_c = \omega_{cp} + \omega_{ce} + \omega_s \tag{5.5}$$

where the surface scattering term is given by

$$\omega_s = \frac{\mathrm{Av}_F}{\left[b(T) - a(T)\right]} \tag{5.6}$$

with v_F being the Fermi velocity of the metal, A is a geometrical factor of unity order of magnitude, and the shell radii as functions of temperature given by $b(T) = b_0\left[1 + \frac{\gamma}{3}\left(T - T_0\right)\right]$, …etc., in terms of the volume expansion of the metal. Thus Eqs. (5.4) – (5.6) provide a model for the temperature dependence of ε, which when used as ε_2 for the nanoshell together with the models in b and c will describe the temperature variation of the optical properties for the nanoshell composite.

5.3 Numerical results

To illustrate the above models, we have studied numerically both the temperature and clustering effects on a composite of silver–glass core shells in a dielectric host of magnesium fluoride: (core/shell/medium) = ($SiO_2 / Ag / MgF_2$). The reference temperature T_0 is set at 293 K, at which the dimensions and concentration of the shells are set with $a = 30$ nm, $b = 50$ nm, and $f_{shell} = 0.01$. The dielectric constants for the core and the host medium are taken as 2.25 and 1.93, respectively, and are assumed constants throughout; and that for the Drude metal can be found from our previous work [52] and references therein. Figure 5.2 shows both the real and imaginary parts of the nanoshell composite at three different temperatures as described by the MG theory. While the dipolar resonances of the composite plasmon modes ($\lambda \approx 400 \text{ nm}$) are clearly seen, they are slightly red-shifted and the corresponding peak dielectric constant values lowered with rise of temperature. This can easily be understood by referring to the lowering of the metallic plasmon frequency due to the decrease in electronic density and increase in electronic damping at high temperatures.

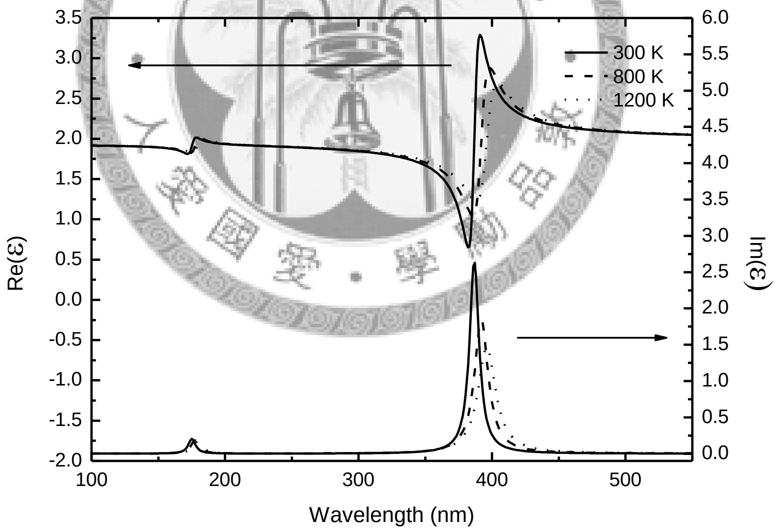

Figure 5.2 Temperature dependence of dielectric function of nanoshell composites in MG distribution. The volume fraction is set at $f = 0.01$, and the aspect ratio is set at $a = 30$ nm and $b = 50$ nm .

The most unique feature of the spectra in Figure 5.2 is the weak resonance appeared at $\lambda \approx 180 \text{ nm}$, which are manifestations of the “single-particle” nanoshell resonance. This has never been seen in a composite of *solid* particle and is unique for the nanoshell composite as can be seen also in the following figures. In the solid particle case, only resonances for the whole composite (i.e. the strong peaks) remain.

To confirm this, we plot in Figure 5.3 (or Figure 5.4 in logarithmic scale) comparison between a composite of solid spheres and shells, and this manifestation of the "single-particle resonances" can be seen only in the shell case with a very minor dependence on the volume fraction of the particles.

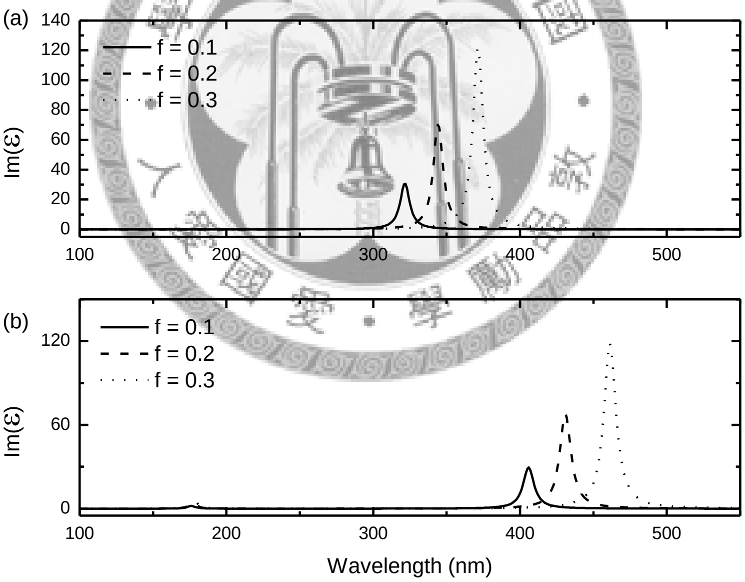

Figure 5.3 The imaginary part of the dielectric functions of (a) solid sphere composites and (b) nanoshell composites in MG distribution with different volume fraction f. The temperatures is fixed at 300 K for all plats.

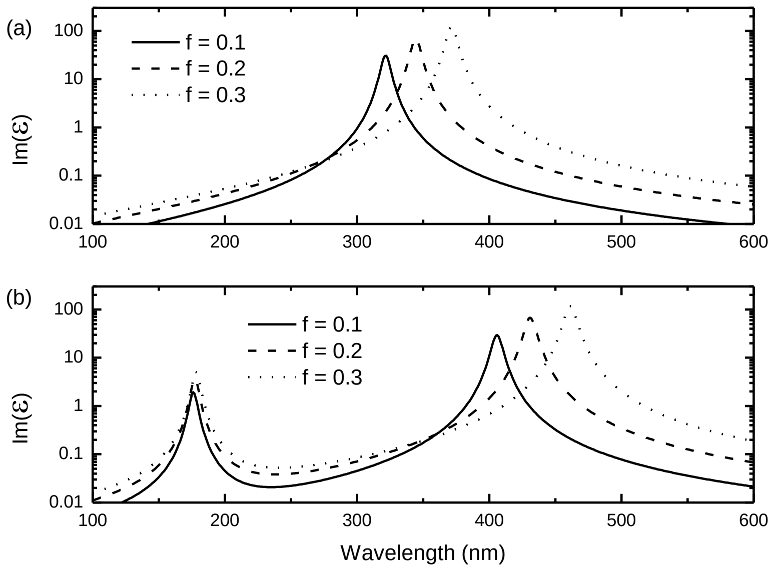

Figure 5.4 Identical to the Figure 5.3 but with logarithmic scale.

Figure 5.5 and Figure 5.6 show how these properties vary when the nanoshells coalesce to form fractal clusters. The temperature is fixed at 300 K. Consistent with what was reported previously in the literature [56], we observe here that particle-clustering among the nanoshells in the composite will lead to appreciable red-shifts in the SP resonance peak – with these shifts more dramatic for lower fractal dimensions (i.e. greater deviation from 3, see Figure 5.5) and larger cluster sizes (see Figure 5.6).

國立臺灣大學

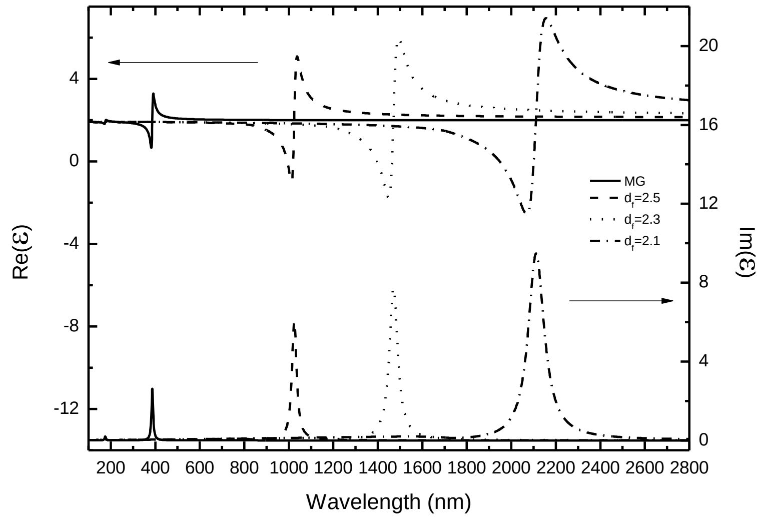

Figure 5.5 Fraction dimension dependence of dielectric functions for nanoshell composites in FC distribution with the same parameters as in Figure 5.2. The cluster radius is fixed at $R = 10b$. The temperature is fixed at 300 K.

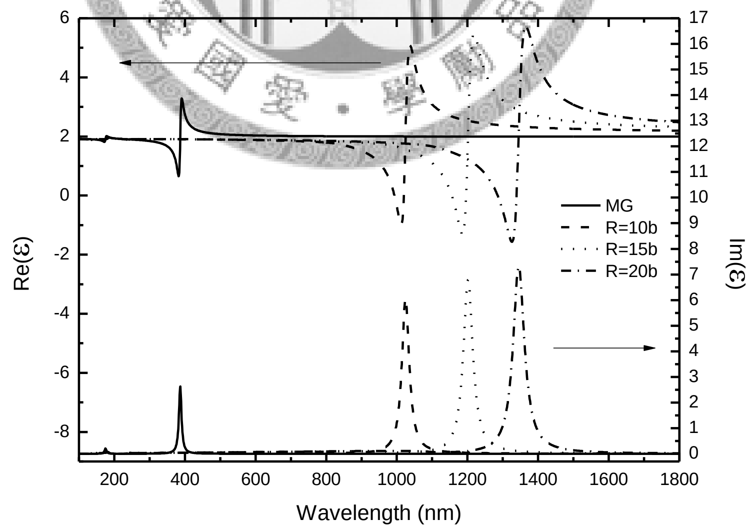

Figure 5.6 Cluster radius dimension dependence of dielectric functions for nanoshell composites in FC distribution with the same parameters as in Figure 5.2. The fractal dimension fixed at $d_f = 2.5$. The temperature is fixed at 300 K.

To possibly observer these changes in the optical properties of the nanoshell composite, we have plotted in Figure 5.7 the transmission spectrum at normal incidence through a thin film made of such composite materials – for both non-clustering (Figure 5.7 (a)) and clustering (Figure 5.7 (b)) cases at three different temperatures. The oscillating patterns shown in Figure 5.7 represent the Fabry-Perot interference of the composite films. Note that in our modeling of the later case, we have assumed both the fractal dimension and cluster size stay unchanged with the rise of temperature, an assumption should be reasonable for the present case with a *solid* host background. While the transmission dips correspond well to the plasmon resonant absorption peaks in the dielectric functions (both single-particle and composite resonances) for both cases, it is observed that the rise in temperature generally decreases the transmission slightly for both materials; and particle-clustering will yield an additional dip in the transmission spectrum near the single-particle resonance frequency.

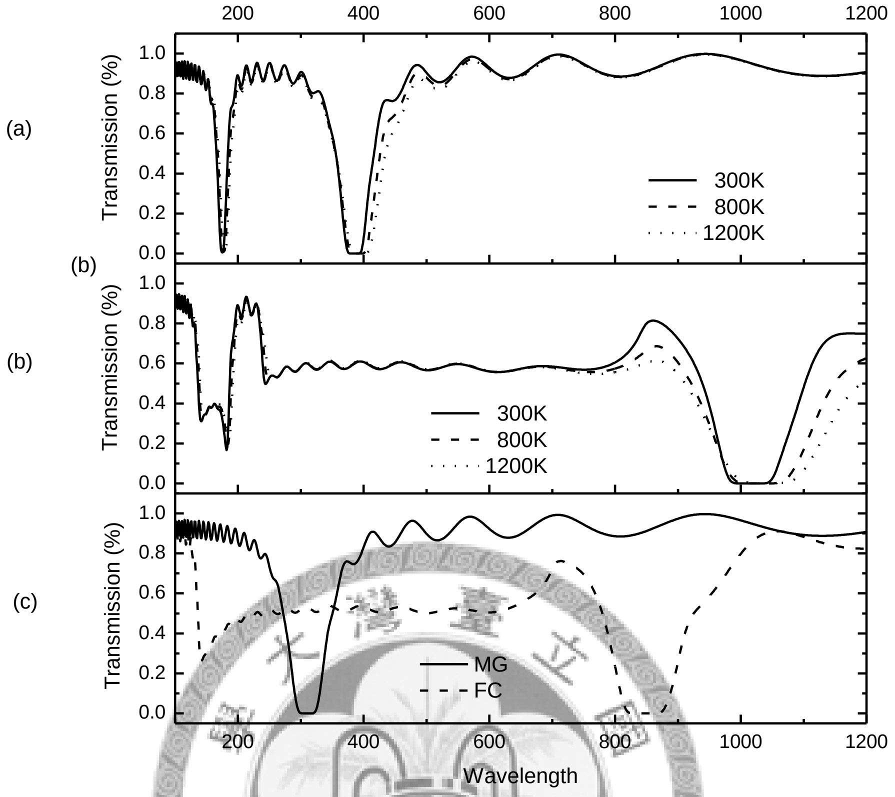

Figure 5.7 The temperature dependence of the transmission spectrum for nanoshell composite films in (a) the MG case and (b) the FC case with the same parameters as in Figure 5.2. (c) The transmission of solid sphere composite films in MG and FC cases. The temperature in (c) is fixed at 300 K and the thicknesses of all films are set at $d = 1\,\mu m$.

It is also shown (Figure 5.7 (c)) how such spectrum for a *solid* particle composite differs from those for the nanoshell composite in the absence of the “single-particle dips”. Note that the additional dip mentioned in Figure 5.7 (b) also appears in Figure 5.7 (c), confirming its origin really from clustering of the particles [56]. From comparison between the results in Figure 5.7 (a) and (b), one observes the effect of particle-clustering according to the FC model is to red-shift the composite resonance (at ~ 400 nm in Figure 5.7 (a)) to a value of ~ 1000 nm in Figure 5.7 (b), and to “create a new resonance” (at ~ 130 nm) near the single-particle resonance wavelength, while leaving this latter resonance almost intact. This can further be confirmed by analyzing the results in Figure 5.7 (c) for a composite of solid particles where no single-resonance exists. As is clear from Figure 5.7 (c), one can observe again that the composite resonance (at ~ 300 nm) is “split” into one at long wavelength (~ 850 nm) and one at short wavelength (~ 130 nm) due to fractal clustering. We have further confirmed that the short wavelength resonances (~ 130 nm in both Figure 5.7 (b) and (c)) are due to the resonance of a *single* cluster (radius R); whereas the long wavelength ones (~ 1000 nm in Figure 5.7 (b) and 850 nm in Figure 5.7 (c)) arise from the characteristic absorptions of the *average* of all these clusters. All the above observations are in consistency with the results reported previously in Ref. [56]. We believe all these new signatures for particle-clustering and shell particles in the composite could be checked against experiments without too much difficulty.

5.4 Conclusion

In this chapter, we have provided a simple model for the description of the optical properties of metallic nanoshell composites. In particular, our model can account for both the temperature and particle-clustering effects on these properties. Among the several interesting results we obtain from our modeling such as red-shifts in plasmon resonances due to either temperature rise or fractal clustering of particles, we regard the most interesting feature revealed from our work is the persistent manifestation of single-particle resonances of the individual nanoshells in the spectra of the dielectric functions. These resonances, while not reported in the previous study of the optical properties of similar core-shell particle composites [48-49], can provide a new signature for the optical probing of this kind of materials.

臺灣大學 國立 · 學 愛國 · 學 勵品 敦 · 人

Chapter 6 Summary and outlook

In this thesis we have focused on the properties of surface plasmon resonance for core-shell particles by using an effective medium model (LSC model). According to this effective medium model we can treat the core-shell particle as an effective solid particle, thus, allowing us to generalize many theories form the solid particle version to the core-shell version.

This effective medium model has been verified to give the exact polarizability in electrostatic situation as demonstrated in chapter 2. This is a consequence of uniqueness property of the boundary value problem in electrostatic theory, which is based on the solution of Laplace equation.

When the particle is very small, typically smaller than 1% of the incident wavelength, we have used LSC model to obtain the exact electrostatic polarizability for spherical and spheroidal core-shell particles. Based on the Drude model for the metallic shell, the split surface plasmon resonance modes are obtained. These split resonance modes are determined by the materials, thickness and geometrical shapes of the core-shell particle. The results obtained from the LSC model are identical to those results from the hybridization model.

After verified the static case, we have extended this model to the electrodynamic case which is required for bigger particles. The wavelength dependence can be introduced by using long-wavelength approximation models such as MLWA and IMLWA. Combining these long-wavelength approximation models with LSC model we have been able to generate the wavelength dependence for the polarizability of the core-shell particle. In comparison with Mie theory, we have verified that this core-shell result generated from LSC model is much better than the static model (i.e. closer to the results from Mie theory).

In the study of the near fields from the plasmonic excitation of the nanoshells, we have studied the FRET process between the two dipoles near a spheroidal nanoshell. Large enhancements for the energy transfer due to surface plasmon resonance of the nanoshell have been observed. In agreement with the hybridization model, we have obtained the multipole resonance peaks which split into two groups corresponding to the two coupled bounding and anti-bounding interfacial plasmon modes. As the results have shown, the dominating modes depend on the positions and orientations of the two dipoles.

Finally, we have also considered the optical properties of metallic nanoshell composites. We have studied the fractal cluster systems with different fractal dimensions and cluster sizes. The results have shown three types of resonances: those from the whole system, those from the individual cluster, and those from the single shells. Among the interesting results from our modeling, a large red-shift was observed with the decrease of the fractal dimension or increase of the cluster size.

Base on the results of this thesis one can propose some further studies. For nanoshell composites we discussed in chapter 5, it will be interest to generalize from spherical to spheroidal nanoshells. It has been thought in the literature that the anisotropic nature of the solid spheroidal particles can be used to enhance the nonlinear response of a composite of these shells [57-62]. It will be interest to study several effects from a composite of these nanoshells.

Another direction is to study the nonlocal effects. Since the local dielectric functions are usually based on the classical oscillator models, they only provide the classical responses. However, for the ultrasmall particles, typically smaller than 10 nm, the quantum effects will become more important and should not be neglected [63-67]. It will be easier to introduce the quantum effects via the nonlocal dielectric function than from solving the quantum mechanical many body Problem. According to the results we presented in this thesis, the LSC model may provide a simple approach to study the nonlocal effects for a system of multi-shell particle.

國立臺灣大學
敦品勵學 · 愛國愛人

Bibliography

1. W. L. Barnes, A. Dereux, and T. W. Ebbesen, *Surface plasmon subwavelength optics*, Nature **424**, 824 (2003)
2. H. Raether, *Surface plasmons on smooth and rough surfaces and on gratings*, Springer-Verlag Berlin Heidelberg (1988)
3. S. A. Maier, *Plasmonics : fundamentals and applications*, New York, Springer (2007)
4. J. B. Jackson and N. J. Halas, *Surface-enhanced Raman scattering on tunable plasmonic nanoparticle substrates*, Proceedings of the National Academy of Sciences of the United States of America **101**, 17930 (2004)
5. K. L. Kelly, et al., *The Optical Properties of Metal Nanoparticles: The Influence of Size, Shape, and Dielectric Environment*, The Journal of Physical Chemistry B **107**, 668 (2002)
6. H. Wang, et al., *Nanorice: A Hybrid Plasmonic Nanostructure*, Nano Letters **6**, 827 (2006)
7. E. Prodan, et al., *A hybridization model for the plasmon response of complex nanostructures*, Science **302**, 419 (2003)
8. D. W. Brandl and P. Nordlander, *Plasmon modes of curvilinear metallic core/shell*

particles, The Journal of Chemical Physics **126**, 144708 (2007)

9. H. Y. Chung, P. T. Leung, and D. P. Tsai, *Dynamic modifications of polarizability for large metallic spheroidal nanoshells*, The Journal of Chemical Physics **131**, 124122 (2009)

10. C. F. Bohren and D. R. Huffman, *Absoption and Scattering of Light by Small Particle*, New York, Wiley (1983)

11. A. Moroz, *Depolarization field of spheroidal particles*, Journal of the Optical Society of America B **26**, 517 (2009)

12. M. Meier and A. Wokaun, *Enhanced fields on large metal particles: dynamic depolarization*, Opt. Lett. **8**, 581 (1983)

13. S. Kawata, *Near-field optics and surface plasmon polaritons*, Springer, Berlin, (2001)

14. J. Li, G. Sun, and C. T. Chan, *Optical properties of photonic crystals composed of metal-coated spheres*, Physical Review B **73**, 075117 (2006)

15. D. Bedeaux and J. Vlieger, *Optical Properties of Surface*. 2nd ed., London, Imperial College Press (2004).

16. C. Flammer, *Spheroidal Wave Functions*, Stanford, California, Stanford University Press (1957)

17. I. S. Gradshteyn and I. M. Ryzhik, *Tables of Integrals, Series and Products*, New

York: Academic Press (1965)

18. P. M. Morse and H. Feshbach, *Methods of Theoretical Physics*. Vol. I and II, New York: McGraw-Hill (1953)

19. C. F. Bohren and D. R. Huffman, *Absoption and Scattering of Light by Small Particle*, New York: Wiley (1953)

20. M. Kerker, *The scattering of light and other electromagnetiv radiation*, New York, Academic (1969)

21. G. Mie, *Beitrage zur Optik truber Medien speziell kolloidaler Metallosungen*, Annalen der Physik **25**, 377 (1908)

22. H. Kang and G. Milton, *Solutions to the Pólya–Szegö Conjecture and the Weak Eshelby Conjecture*, Archive for Rational Mechanics and Analysis **188**, 93 (2008)

23. A. Wokaun, J. P. Gordon, and P. F. Liao, *Radiation Damping in Surface-Enhanced Raman Scattering*, Physical Review Letters **48**, 957 (1982)

24. B. T. Draine and P. J. Flatau, *Discrete-dipole approximation for scattering calculations*, J. Opt. Soc. Am. A **11**, 1491 (1994)

25. H. Mertens, A. F. Koenderink, and A. Polman, *Plasmon-enhanced luminescence near noble-metal nanospheres: Comparison of exact theory and an improved Gersten and Nitzan model*, Physical Review B **76**, 115123 (2007)

26. W.-H. Yang, G. C. Schatz, and R. P. Van Duyne, *Discrete dipole approximation for*

calculating extinction and Raman intensities for small particles with arbitrary shapes, The Journal of Chemical Physics **103**, 869 (1995)

27. E. J. Zeman and G. C. Schatz, *An accurate electromagnetic theory study of surface enhancement factors for silver, gold, copper, lithium, sodium, aluminum, gallium, indium, zinc, and cadmium*, The Journal of Physical Chemistry **91**, 634 (1987)

28. A. F. Stevenson, *Solution of Electromagnetic Scattering Problems as Power Series in the Ratio (Dimension of Scatterer)/Wavelength*, Journal of Applied Physics **24**, 1134 (1953)

29. A. F. Stevenson, *Electromagnetic Scattering by an Ellipsoid in the Third Approximation*, Journal of Applied Physics **24**, 1143 (1953)

30. T. Förster, *10th Spiers Memorial Lecture. Transfer mechanisms of electronic excitation*, Discussions of the Faraday Society **27** (1959)

31. T. Förster, *Zwischenmolekulare Energiewanderung und Fluoreszenz*, Annalen der Physik **437**, 55 (1948)

32. L. Stryer, *Fluorescence Engergy-Transfer as a Spectroscopic Ruler*, Annual Review of Biochemistry **47**, 819 (1978)

33. M. Moskovits, *Surface-Enhanced Spectroscopy*, Reviews of Modern Physics **57**, 783 (1985)

34. S. K. Gray, *Surface Plasmon-Enhanced Spectroscopy and Photochemistry*, Plasmonics **2**, 143 (2007)

35. S. Kuhn, et al., *Enhancement of single-molecule fluorescence using a gold nanoparticle as an optical nanoantenna*, Physical Review Letters **97**, 017402 (2006)

36. P. Andrew and W. L. Barnes, *Forster Energy Transfer in an Optical Microcavity*, Science **290**, 785 (2000)

37. F. Reil, et al., *Förster-Type Resonant Energy Transfer Influenced by Metal Nanoparticles*, Nano Letters **8**, 4128 (2008)

38. X. M. Hua, J. I. Gersten, and A. Nitzan, *Theory of energy transfer between molecules near solid state particles*, The Journal of Chemical Physics **83**, 3650 (1985)

39. C. A. Marocico and J. Knoester, *Intermolecular resonance energy transfer in the presence of a dielectric cylinder*, Physical Review A **79**, 053816 (2009)

40. H. Y. Xie and et al., *Plasmonic enhancement of Förster energy transfer between two molecules in the vicinity of a metallic nanoparticle: Nonlocal optical effects*, Physical Review B **80**, 155448 (2009)

41. M. Durach and et al., *Nanoplasmonic renormalization and enhancement of Coulomb interactions*, New Journal of Physics **10**, 105011 (2008)

42. J. Zhang, et al., *Enhanced Förster Resonance Energy Transfer on Single Metal Particle. 2. Dependence on Donor−Acceptor Separation Distance, Particle Size, and Distance from Metal Surface*, The Journal of Physical Chemistry C **111**, 11784 (2007)

43. J. Zhang, Y. Fu, and J. R. Lakowicz, *Enhanced Förster Resonance Energy Transfer (FRET) on a Single Metal Particle*, The Journal of Physical Chemistry C **111**, 50 (2006)

44. S. J. Oldenburg, et al., *Nanoengineering of optical resonances*, Chemical Physics Letters **288**, 243 (1998)

45. L. Hirsch, et al., *Metal Nanoshells*, Annals of Biomedical Engineering **34**, 15 (2006)

46. S. Lai, et al., *Tailoring plasmonic substrates for surface enhanced spectroscopies*, Chen. Soc. Rev. **37**, 898 (2008)

47. C. Tserkezis and et al., *Collective plasmonic modes in ordered assemblies of metallic nanoshells*, Journal of Physics: Condensed Matter **20**, 075232 (2008)

48. A. V. Goncharenko, *Optical properties of core-shell particle composites. I. Linear response*, Chemical Physics Letters **386**, 25 (2004)

49. A. V. Goncharenko and Y.-C. Chang, *Optical properties of core-shell particle composites. II. Nonlinear response*, Chemical Physics Letters **439**, 121 (2007)

50. S. R. Sershen, et al., *Temperature-sensitive polymer-nanoshell composites for photothermally modulated drug delivery*, Journal of Biomedical Materials Research **51**, 293 (2000)

51. Y. M. Wu and G. Q. Chen, *Effect of temperature on optical bistability of coated granular composites*, Wuli Xuebao/Acta Physica Sinica **58**, 2056 (2009)

52. C. W. Chen, et al., *Temperature dependence of enhanced optical absorption and Raman spectroscopy from metallic nanoparticles*, Solid State Communications **148**, 413 (2008)

53. H. P. Chiang, P. T. Leung, and W. S. Tse, *Optical properties of composite materials at high temperatures*, Solid State Communications **101**, 45 (1997)

54. J. C. Maxwell Garnet, Philos. Trans. R. Soc. London. Ser: A **203**, 385 (1904)

55. J. C. Maxwell Garnet, Philos. Trans. R. Soc. London. Ser: A **205**, 237 (1906)

56. P. M. Hui and D. Stroud, *Complex dielectric response of metal-particle clusters*, Physical Review B **33**, 2163 (1986)

57. L. Gao and et al., *Effective non-linear optical properties of metal-dielectric composites of spheroidal particles*, Journal of Physics: Condensed Matter **12**, 6825 (2000)

58. K. P. Yuen, M. F. Law, K. W. Yu and P. Sheng, *Optical nonlinearity enhancement via geometric anistropy*, Phys. Rev. E, **56**, R1322 (1997)

59. C. Flytzanis, F. Hache, M. C. Klein, D. Richard and P. Roussignol, Prog. Opt, **29**, 323 (1991)

60. D. Stroud and V. E. Wood, *Decoupling approximation for the nonlinear-optical response of composite media*, J. Opt. Soc. Am. B, **6**, 778 (1989)

61. J. W. Haus, N. Kalyaniwalla, R. Inguva, M. Bloemer, and C. W. Bowden, *Nonlinear-optical properties of conductive spheroidal particle composites*, J. Opt. Soc. Am. B, **6**, 797 (1989)

62. C. M. Bowden, C. C. Sung, J. W. Haus, and J. M. Cook, *Longitudinal spatial inhomogeneities in intrinsic optical bistability due to induced absorption*, J. Opt. Soc. Am B, **5**, 11 (1988)

63. H. Y. Xie, et al., *Plasmonic enhancement of F&ouml;rster energy transfer between two molecules in the vicinity of a metallic nanoparticle: Nonlocal optical effects*, Physical Review B **80**, 155448 (2009)

64. R. Chang and P. T. Leung, *Nonlocal effects on optical and molecular interactions with metallic nanoshells*, Physical Review B **73**, 125438 (2006)

65. J. Vielma and P. T. Leung, *Nonlocal optical effects on the fluorescence and decay rates for admolecules at a metallic nanoparticle*, The Journal of Chemical Physics **126**, 194704-7 (2007)

66. B. B. Dasgupta and R. Fuchs, *Polarizability of a small sphere including nonlocal*

effects, Physical Review B **24**, 554 (1981)

67. R. Rojas, F. Claro, and R. Fuchs, *Nonlocal response of a small coated sphere*, Physical Review B **37**, 6799 (1988)